Noname manuscript No.
(will be inserted by the editor)

Impact of tumor-parenchyma biomechanics on liver metastatic progression: a multi-model approach

Yafei Wang[1,2] · **Erik Brodin**[2,3] · **Kenichiro Nishii**[3] · **Hermann B. Frieboes**[4] · **Shannon Mumenthaler**[5] · **Jessica L. Sparks**[3,†] · **Paul Macklin**[1,‡]

Received: date / Accepted: date

Abstract Colorectal carcinoma (CRC) and other cancers often metastasize to the liver in later stages of the disease, contributing significantly to patient death. While the biomechanical properties of the liver parenchyma (normal liver tissue) are known to affect primary and metastatic tumor growth in liver tissues, the role of these properties in driving or inhibiting metastatic inception remains poorly understood. This study uses a multi-model approach to study the effect of tumor-parenchyma biomechanical interactions on metastatic seeding and growth; the framework also allows investigating the impact of changing tissue biomechanics on tumor dormancy and "reawakening."

We employ a detailed poroviscoelastic (PVE) model to study how tumor metastases deform the surrounding tissue, induce pressure increases, and alter interstitial fluid flow in and near the metastases. Results from these short-time simulations in detailed single hepatic lobules motivate constitutive relations and biological hypotheses for use in an agent-based model of metastatic seeding and growth in centimeter-scale tissue over months-long time scales.

We find that biomechanical tumor-parenchyma interactions on shorter time scales (adhesion, repulsion, and elastic tissue deformation over minutes) and longer time scales (plastic tissue relaxation over hours) may play a key role in tumor cell seeding and growth within liver tissue. These interactions may arrest the growth of micrometastases in a dormant state and can prevent newly

[1]Department of Intelligent Systems Engineering, Indiana University. Bloomington, IN USA
[2]Contributed equally to this work
[3]Department of Chemical, Paper and Biomedical Engineering, Miami University. Oxford, OH USA
[4]Department of Bioengineering, James Graham Brown Cancer Center, and Center for Predictive Medicine, University of Louisville. Louisville, KY USA
[5]Lawrence J. Ellison Institute for Transformative Medicine, University of Southern California. Los Angeles, CA USA
[†]Corresponding author for poroviscoelastic model. E-mail: sparksj6@MiamiOH.edu
[‡]Corresponding author for agent-based model and overall study.
E-mail: macklinp@iu.edu

arriving cancer cells from establishing successful metastatic foci. Moreover, the simulations indicate ways in which dormant tumors can "reawaken" after changes in parenchymal tissue mechanical properties, as may arise during aging or following acute liver illness or injury. We conclude that the proposed modeling approach can yield insight into the role of tumor-parenchyma biomechanics in promoting liver metastatic growth, with the longer term goal of identifying conditions to clinically arrest and reverse the course of late-stage cancer.

Keywords Poroviscoelastic model · Agent-based model · Biomechanics · Tumor-tissue interaction

1 Introduction

The most common site for cancer metastases to spread are the lymph nodes and the liver. While lymph nodes may be resectable, the liver is a vital organ to which metastatic spread cannot be cured. Liver metastases thus represent a terminal stage of the disease for several major cancers, including breast, prostate, lung, pancreas, colon, and melanoma. In particular, over 50,000 people annually die in the U.S. from metastatic (Stage IV) colorectral cancer (CRC) [1]. The most common metastatic site is the liver, with more than half of patients affected, while the lungs are the second most common location (10-20% of patients). Although resection of liver tissue yields the best outcome (5-year survival rate 35% to 58%), over 80% of patients are ineligible due to health issues or the size/location of the lesions. Fluorouracil, typically combined with leucovorin and irinotecan (or oxaliplatin), has been the standard chemotherapeutic treatment for metastatic CRC, for which the 5-year survival rate is a dismal 14% even after therapeutic intervention [1].

Tissue stiffness, extracellular matrix (ECM) composition and fiber alignment, and other biomechanical factors are known to affect primary and metastatic tumor growth [2, 3]. In liver tissues, prior injuries and diseases such as cirrhosis increase fibrosis, and alter tissue stiffness [3]. Aging may also contribute to changes in liver tissue stiffness, as well as increase the likelihood of tissue fibrosis following an acute injury or illness [4–6].

The literature on the effect of such biomechanical alterations on tumor growth in the liver is seemingly inconsistent: some report low incidence of CRC metastases in cirrhotic livers (with accompanying fibrosis) [7], while others have reported that the risk of CRC liver metastases may be higher in patients with cirrhosis [8]. Still others report that stiff tissues can promote tumor growth and metastasis in the liver (e.g., [9]). Some of these conflicting reports may lie in the difference between *invasion* from a primary site at the start of the metastatic cascade (generally characterized as epithelial-mesenchymal transition, or EMT) and *seeding and growth* at a metastatic site (mesenchymal-epithelial transition, or MET) [10]. In EMT, tissue stiffness can up-regulate cell motility and matrix remodeling [11, 12], whereas stiff tissues at a metastatic site may impair tumor growth following MET [10].

Indeed, metastatic "seeds" arriving in a new "soil" may rest dormant for many years: a seeded metastasis may cease proliferating at a small, sub-clinical size or fail to grow at all; unknown later events may "reawaken" long-dormant metastases to resume rapid growth [12]. While there has been some prior study of the molecular-level triggers for metastatic reawakening (e.g., see discussion in [12]), far less is understood of the potential role of direct tumor-parenchyma mechanical interactions, or how mechanical changes following injury, illness, or aging could drive a dormant micrometastasis back to a rapidly growing state. Similarly, most investigations of age-driven changes in liver tissue have focused on immunologic and molecular-scale changes to ECM, rather than to broader mechanical properties (e.g., see [13]).

A more detailed understanding of mechanobiological feedbacks between a seeded micrometastasis and the surrounding parenchyma is required to help detangle these inconsistent observations. To arrive at this detailed understanding, we need to investigate how growing micrometastases disrupt interstitial fluid flow and impose mechanical pressures on the surrounding parenchyma, how these lead to parencyhma deformation and death, and how tumor-parenchyma mechanical interactions can alter tumor cell proliferation. With an improved understanding of these links, we could identify critical events most likely to drive emergence of new liver metastases in CRC patients, and thereby tailor more appropriate monitoring and early interventions for these at-risk patients.

The limitations inherent in experimental effort pursuing this understanding, including the artificial environment of *in vitro* setups and the confounding interactions present in *in vivo* models, may be addressed via mathematical modeling and computational simulation, which provide for the means to perform systematic analyses. This work seeks to establish a platform to pursue detailed evaluation of cell-stromal interactions and the associated tissue-scale effects within the context of the liver. In the longer term, such a platform could enable evaluating potential metastatic spread and progression based on patient-specific tumor cell and liver tissue characteristics.

1.1 Background biology

The liver is a vital organ that performs critical physiological processes such as macronutrient metabolism, bile creation, and filtration of toxic substances from the blood [14]. Liver cell types, including hepatocytes, cholangiocytes, stellate cells, Kupffer cells, and liver sinusoidal endothelial cells are organized in an intricate and complex architecture. The main structural units are the hepatic lobules, within which hepatocytes are arranged in a hexagonal pattern around the central vein. The portal triads, consisting of the hepatic artery, portal vein, and bile duct, are found at the vertices of these hepatic lobules. See Fig. 1. Fluid transport occurs via liver sinusoids, which are lined by thin, fenestrated endothelial cells, and allow for mixing of oxygen-rich blood from the hepatic artery with nutrient-rich blood from the portal vein [15]. This leads

to the formation of oxygen, nutrient, and waste gradients across the sinusoids, resulting in lobule regions where distinct metabolic processes occur termed "metabolic zonation".

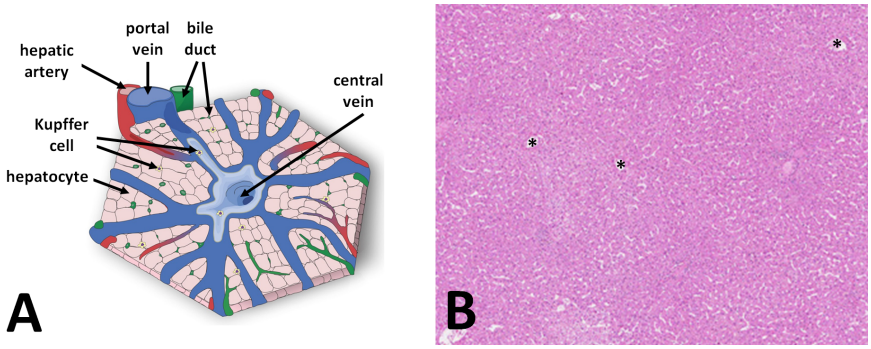

Fig. 1 **A:** Schematic of a typical liver lobule. Adapted under CC BY-NC 4.0 from [16]. **B:** Typical human liver histology (hematoxylin and eosin staining), with several central veins marked with *. Adapted under CC BY-SA 3.0 from the Human Protein Atlas available from http://www.proteinatlas.org [17].

While the liver is critically involved in normal physiological functions, it can also be a common site for metastatic disease. Liver metastases are a major barrier in cancer management. In particular, for CRC, patient mortality is principally due to the spread of disease to distant organs, with the liver being the predominant site in approximately 70% of the cases. This metastatic organotropism is mainly attributed to the drainage of the colon and rectum blood supply directly into the liver through the portal vein. Tumor cells that survive and proliferate in the liver microenvironment do so by replacing resident hepatocytes, co-opting the vasculature, adhering to hepatocyte-derived extracellular matrix (ECM), and communicating with neighboring stromal cells [18]. The reciprocal interactions between resident (liver parenchyma) and recruited (inflammatory and immune) cells in the liver microenvironment govern the successful formation of metastatic tumor foci. Significant research has focused on the molecular alterations leading to metastatic disease, yet the biophysical and biochemical interactions between tumor cells and the metastatic microenvironment remain to be fully elucidated with the goal to improve therapeutic interventions and patient outcomes.

1.2 Prior mathematical modeling work

While there have been numerous modeling advances in related areas, to the best of our knowledge, no model has been developed to address tumor-parenchyma biomechanical feedback in large tissues and the impact on tumor growth and parenchyma disruption. This section briefly introduces key prior work; please see Appendix A for an expanded overview of the prior work.

There is a rich history of mathematical modeling of liver biology, particularly liver tissue regeneration [19, 20], liver fibrosis [21, 22], liver toxicology [23, 24], interstitial flow and mechanics in liver tissues [25–31]. Others have modeled the role of tissue mechanics on (mostly primary) tumor growth [32–35], including some excellent work on the role of mechanosensing in tumor cell proliferation [36, 37], although these did not focus specifically on primary or metastatic tumor growth in liver tissues.

While there is less history in specific modeling of liver metastases, some have modeled the growth of metastases in the liver [38–40], while others have simulated the impact of extracellular matrix (ECM) remodeling and macrophages in liver metastases [41–43]. There are also good examples of simulating nanotherapy treatments [44–46] and theranostics [47, 48] of liver metastases. Others have developed network models of metastatic seeding [49–54], but without spatiotemporal detail and without considering the impact of tumor-host biomechanical interactions.

In spite of these extensive empirical and mathematical modeling efforts, the impact of parenchymal mechanics and flow on metastatic growth in the liver remain poorly understood, as is the biology regulating tumor-parenchyma interactions near the tumor boundary.

And while emerging microfluidic "lab on a chip" platforms (e.g., [55]) and microphysiological systems (e.g., [56]) allow evaluation of some of these dynamics, it remains difficult to measure flow dynamics at small scales, especially in and around incipient metastatic foci. Past multiscale modeling investigations (including those discussed above) have mainly focused on discrete or smaller-scale simulations to provide insights at larger, continuum scales, including tissue regeneration, toxicology, and single-scale flow modeling. However, none have investigated cell-level mechanobiologic effects over large tissues, nor have they been motivated by detailed continuum models of interstitial flow to drive efficient whole-tissue scale models over long times.

1.3 Key effects to investigate

The modeling framework presented here will allow probing these knowledge gaps, with a focus on (1) evaluating whether disrupted interstitial flow significantly slows tumor growth by limiting the availability of cell oxygen and nutrients, (2) determining if mechanical pressure feedbacks on tumor cell proliferation are necessary to avoid non-physical model behaviors, (3) identifying the conditions under which parenchymal biomechanics results in tumor dormancy, and (4) evaluating whether changes in parenchymal biomechanics (e.g., from aging, injuries, or acute disease) can reawaken a dormant tumor.

1.4 Overall modeling approach

We combine two modeling approaches to investigate metastatic tumor seeding and growth in liver tissues. A high-resolution poroviscoelastic (PVE) model

of interstitial flow and tissue mechanics gives detailed insights on a tumor's impact on interstitial flow, transport, mechanical pressure, and tissue deformation in and around a tumor micrometastasis for a quasi-steady tumor on short time scales. We use an efficient, lattice-free agent-based model (ABM) framework to simulate individual CRC cells and parenchyma agents in centimeter-scale liver tissues over weeks and months.

Unlike typical matched models where small-scale discrete models motivate large-scale continuum models, this study uses a detailed continuum model of flow mechanics to generate hypotheses and simplifications for scalable discrete models. We use the PVE model results to build constitutive relations for growth substrate transport at centimeter scale, in tissues with hundreds of lobules. We also use the PVE results to motivate biological rules (hypotheses) to study tumor tumor cells and parenchymal tissue in a centimeter-scale agent-based model (ABM) of tumor metastatic growth in liver tissue. The multi-model framework is summarized in Fig. 2.

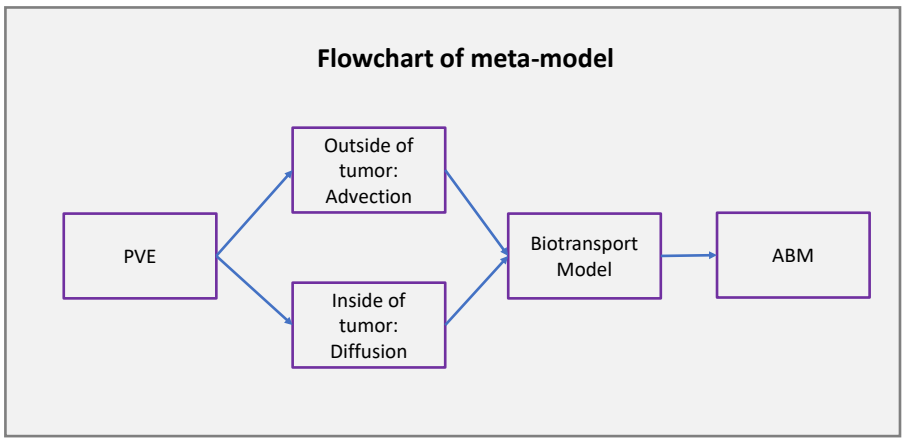

Fig. 2 Modeling framework implemented in this study to evaluate the impact of liver tissue mechanobiology on metastatic seeding and progression

2 Materials and methods

2.1 Poroviscoelastic (PVE) Model

This section illustrates the theoretical details of the PVE model, model assumptions, computational domain and numerical implementation details. The material properties and boundary conditions as well as fluid velocity, strain, stress, and pore fluid pressure results are included in the Supplementary Materials.

2.1.1 PVE model overview

A detailed mathematical description of the mechanics of poroviscoelastic materials was published by [57], and the application of poroviscoelastic models to liver tissue has been demonstrated by [58–60] among others. The summary given here is adapted from [30, 60, 61]. A biphasic material consists of a linear elastic solid phase and an incompressible fluid phase, where relative motion between the two phases produces rate-dependent (i.e. viscoelastic) behavior [62]. If the fluid phase is inviscid, biphasic theory is equivalent to poroelasticity. Poroviscoelasticity extends poroelasticity by modeling the solid phase as viscoelastic, rather than linear elastic [63]. Equations 1-7 comprise biphasic material mechanics, Equations 8 and 9 provide for viscoelasticity of the solid phase, and Equations 10 and 11 finish the constitutive description.

The conservation of mass for incompressible solid and fluid phases can be written as:

$$\nabla \cdot \left(\phi^s v^s + \phi^f v^f\right) = 0 \tag{1}$$

where s and f indicate solid and fluid phase, respectively, ϕ^s and ϕ^f are solid and fluid volume fractions, and v is velocity. If inertial forces are negligible compared with internal frictional forces, the conservation of linear momentum can be written as:

$$\nabla \cdot T^f + \Pi^f = 0 \tag{2}$$

$$\nabla \cdot T^s + \Pi^s = 0 \tag{3}$$

where T^f and T^s are Cauchy stress tensors and Π^f and Π^s are viscous drag forces arising from the interaction between the fluid and solid phases. Π^f and Π^s are proportional to their relative velocities and inversely proportional to hydraulic permeability, k:

$$\Pi^s = -\Pi^f = \frac{\left(\phi^f\right)^2}{k}\left(v^f - v^s\right) \tag{4}$$

Stress tensors in the fluid and solid phases can be written as:

$$T^f = -\phi^f p I \tag{5}$$

$$T^s = -\phi^s p I + \widetilde{T}^s \tag{6}$$

where p is hydrostatic pressure and $\widetilde{T}^s$ is apparent solid stress due to solid matrix deformation [62–64].

If the solid phase is linear elastic, then $\widetilde{T}^s$ can be written as:

$$\widetilde{T}^s = \lambda E_{kk} I + 2\mu E \tag{7}$$

where E is the infinitesimal strain tensor and λ and μ are Lamé constants. To account for intrinsic viscoelasticity of the solid phase, the solid stress tensor can be replaced with:

$$\widetilde{T}^s = \int_0^a 2G\left(\tau - \tau'\right)\dot{e}dt' + I\int_0^t K\left(\tau - \tau'\right)\dot{\phi}dt \tag{8}$$

where G and K are elastic shear and bulk relaxation functions, e is deviatoric strain, and φ is volumetric strain [63][64]. The relaxation functions can be defined by a Prony series expansion

$$R(t) = \frac{R_\infty}{1 - \sum_{i=1}^{n} r_i} \left[1 - \sum_{i=1}^{n} r_i \left(1 - e^{-\frac{t}{\tau_i}} \right) \right] \tag{9}$$

where R is the time-dependent modulus, R_∞ is the long-term modulus, and n, r_i, τ_i are Prony series constants. In the Abaqus implementation in the present work, the material behavior was defined by specifying the hydraulic conductivity (K), the specific weight of the liquid (γ), the Prony series constants, a long-term Young's modulus (E_∞), and Poisson's ratio (ν) so that:

$$G_\infty = \frac{E_\infty}{2(1-\nu)} \tag{10}$$

$$k = \frac{K}{\gamma} \tag{11}$$

2.1.2 Starting model assumptions

It is assumed that necrosis is a source of fluid pressure as necrotic cells release fluid. It is also assumed that proliferating cells are a fluid pressure sink, as proliferating cells grow in part by absorbing fluid. Accordingly, the medium (400 μm diameter) tumor is considered as a net pressure source, reflecting a release of fluid from the necrotic core that exceeds the uptake of fluid by cells in the viable rim. For comparison, in a different model iteration the medium tumor is considered as neutral, neither a source nor a sink, to reflect the possible condition that fluid release and fluid uptake are in balance. The small (200 μm diameter) tumor is considered as a net pressure sink reflecting more proliferation than necrosis. Lastly, the tumor seed (50 μm diameter) was considered as neutral, as a tumor of this size would consist of only a few cells and its contribution as a fluid source or sink may be neglected.

2.1.3 Model geometry

Model geometry is given in Fig. 3. Lobule dimensions and vessel radii (Table 1) were obtained from histological images in published literature [65–68]. Dimensions for ℓ and h are reported as the distance between the centers of the pre-tPVs (pre-terminal portal veins), and d is reported as the farthest distance between model faces in the z and -z direction. Each quarter-lobule model contained from 299,258 to 677,457 quadratic tetrahedral elements (Abaqus element type C3D10MP). Simulation time was 150 seconds and the minimum time step was 0.15 seconds.

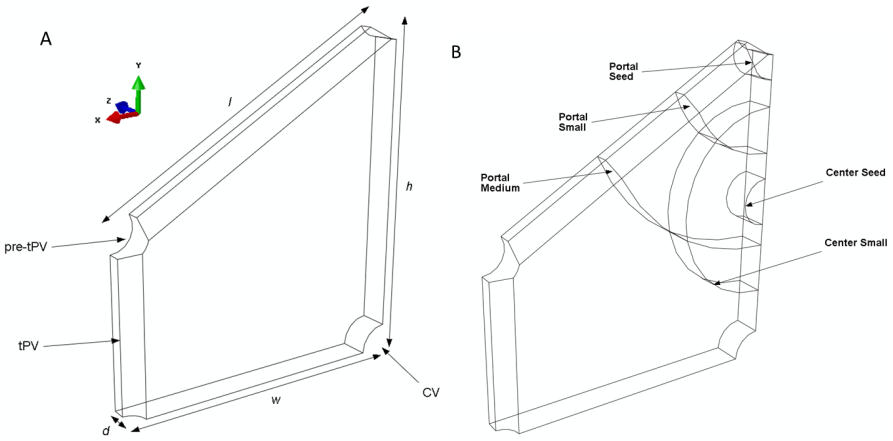

Fig. 3 The PVE computational model. Model geometry (**A**) and simulated tumor sizes and positions (**B**). (**A**) Quarter liver lobule showing locations of the pre-terminal portal vein (pre-tPV), terminal portal vein (tPV), and central vein (CV). Dimensions ℓ, w, h, and d are given in Table 1. (**B**) Tumors of different sizes (seed, small, medium) were simulated for different lobule locations, including the midpoint of the central-portal axis (termed the "center" position) and in the portal triad (termed the "portal" position).

Table 1 Quarter lobule dimensions adapted from Nishii et al. [30]

Dimensions (μm)	
CV radius	26.5
tPV radius	16
pre-tPV radius	23
Edge length (l)	350
Edge width (w)	303.1
Edge height (h)	350
Lobule depth (d)	30

2.1.4 Numerical implementation

In order to model the liver microenvironment, a three-dimensional poroviscoelastic finite element model of a quarter liver lobule (Fig. 3) was created in Abaqus (v6.12, 3DS Dassault Systems, Waltham, MA), modified from the prior work of Nishii et al [30]. A poroviscoelastic material model was selected because this constitutive description of liver tissue mechanics has been shown to capture the viscoelastic stress-strain behavior of the solid matrix as well as pressure-driven flow of fluid through the matrix pores [30]. To reduce computational time, only one-fourth of the hexagonal lobule geometry was simulated, and symmetry boundary conditions were applied to X, Y and Z planes (Fig. 3). Model thickness in the Z direction was set to 30 μm to approximate the diameter of one hepatocyte. Dimensions and parenchyma material properties were obtained from literature [30] as described above. Once the base model geometry was established (Fig. 3A), three different sized tumors denoted as seed (50 μm diameter), small (200 μm diameter), and medium (400 μm di-

ameter) tumors were included. Tumors were also modeled as poroviscoelastic solids, but with greater stiffness and altered hydraulic conductivity compared with normal parenchyma (these material properties are described in Supplementary Materials). Tumors were placed at the midpoint of the central-portal axis (termed the "center" position) and in the portal triad (termed the "portal" position). Tumor sizes and locations are shown in Fig. 3B. Each model run simulated only one tumor size at one location.

2.2 Biotransport modeling in BioFVM

In [69], Macklin and coworkers developed *BioFVM* to simulate diffusive biotransport for large 2-D and 3-D biological problems with off-lattice, cell-based sources and sinks. Specifically, if $\boldsymbol{\rho}$ is a vector of diffusible substrates with diffusion coefficients $\boldsymbol{D}$, decay rates $\boldsymbol{\lambda}$, bulk source rates $\boldsymbol{S}$ (which saturate at target densities $\boldsymbol{\rho^*}$), and bulk uptake rates $\boldsymbol{U}$, then problems of the following form are solved:

$$\begin{aligned}\frac{\partial \boldsymbol{\rho}}{\partial t} &= \boldsymbol{D}\nabla^2\boldsymbol{\rho} - \boldsymbol{\lambda}\boldsymbol{\rho} + \boldsymbol{S}(\boldsymbol{\rho}^* - \boldsymbol{\rho}) - \boldsymbol{U}\boldsymbol{\rho} \\ &\quad + \sum_{\{\text{cells } i\}} \delta(\boldsymbol{x} - \boldsymbol{x}_i) W_i [\boldsymbol{S}_i(\boldsymbol{\rho}_i^* - \boldsymbol{\rho}) - \boldsymbol{U}_i\boldsymbol{\rho}].\end{aligned} \tag{12}$$

with Neumann (zero flux) boundary conditions. Here, for a collection of cells (indexed by i), with centers $\mathbf{x}_i$ and volumes W_i, their secretion rates are $\mathbf{S}_i$ (with saturation densities $\boldsymbol{\rho_i^*}$) and their uptake rates are $\mathbf{U}_i$.

The method tested second-order accurate in space, first-order accurate in time, and numerically stable in typical parameter regimes for cancer and tissue biology. The method was tested for scalability on systems of millions of off-lattice agents, millinos of voxels, and dozens of diffusing substrates. Setting $\Delta t = 0.01$ min and $\Delta x = 20\,\mu$m maintained relative errors below 5% for diffusion, decay, uptake, and source rates typical for cancer and tissue biology. See [69] for full details on the numerical method, implementation, and convergence testing. In [70], BioFVM is used as the default biotransport solver, with the system performed accurately and stably even on systems of moving cells.

A useful feature of BioFVM are *Dirichlet nodes*: any voxel j centered at position $\mathbf{x}_j$ can have its substrate values set to $\boldsymbol{\rho}_j$ to approximate Dirichlet conditions on arbitrary geometries. Moreover, one can set or unset any computational voxel as a Dirichlet node at any simulation time, or overwrite the values of $\boldsymbol{\rho_j}$. This feature will be used in Section 3.4 to approximate quasi-steady conditions in selected tissue regions.

2.3 Multicellular modeling in PhysiCell

In [70], Macklin and coworkers developed *PhysiCell* for off-lattice agent-based simulations in multicellular systems biology, with a particular focus on cancer. Each cell is a software agent that moves under the balance of mechanical

forces under the "inertialess" assumption as in earlier work by Drasdo, Höhme and colleagues [71]. Each cell agent with index i has a phenotype $\mathbf{P}_i$: a hierarchically structured set of properties including state and rate parameters for cell cycling, death, volume changes, motility, mechanics, and secretion/uptake. Each cell can sample the microenvironment (modeled with BioFVM; see Section 2.2) and any element of $\mathbf{P}_i$ based upon these local microenvironmental conditions. Each cell agent can have custom functions assigned to it; extensive use of these functions is made to model custom mechanobiology in Section 3.4. PhysiCell has been extensively tested on a variety of multicellular systems problems with 10^5 to 10^6 cells. Its computational cost scales linearly with the domain size and number of simulated agents. See [70] for full algorithmic detail, numerical testing, and a variety of examples.

2.3.1 Implementation details

In this paper, we used PhysiCell Version 1.2.1 [70] with two agent types: tumor cells (individual cancer cells arriving to colonize and grow in the parenchyma) and parenchyma agents (small portions of parenchyma tissue). For this study, we do not model the fine lobular structure (particularly hepatic cords and sinusoids), but this is a continuing topic of interest for future study.

We use the built-in "Ki67 Advanced" cell cycle model (with default parameters), where quiescent Ki67- cells can transition to a pre-mitotic Ki67+ state, grow, and divide into two Ki67+ daughter cells. These daughter cells grow and exit the cycle to the Ki67- state. Each cell can grow, apoptose, or necrose based upon user-defined functions. Except as described later, we use the standard, built-in cell mechanics. We also begin the built-in oxygen-dependent proliferation and necrosis: notably, the Ki67- to Ki67+ transition rate increases with oxygen availability above a minimal hypoxic threshold, and the necrotic death rate increases below the threshold. See [70] for further details and default parameter values.

For parenchyma agents, we set cycling and apoptosis to zero to model a homeostatic tissue in the absence of tumor cells. This investigation does not focus on single-cell invasion and EMT, but rather post-MET metastatic seeding and growth; we disable cell motility accordingly. The full source code is available as open source (see Appendix D), and an interactive, online version can be run at https://nanohub.org/tools/pc4livermedium.

2.4 Generating large 2-D virtual liver tissues

This study required large 2-D (thin 3-D) sections of virtual liver tissue. Here, we describe a straightforward approach to generate a synthetic tissue dataset, based upon a Voronoi approximation of hepatic lobule packing. To generate a large liver tissue:

1. Central veins (CVs) are randomly placed across the tissue, with mean density $\sim 2 \times 10^{-6} \mu\text{m}^{-2}$ (to ensure a mean hepatic lobular diameter of

approximately 800 μm, similar to analyses in whole-lever models such as [30, 67]);
2. Any closely-spaced pairs of CVs are replaced with a single CV placed at their midpoint; and
3. Remaining space is filled with (hexagonally-packed) parenchymal agents.

As needed, the lobular boundaries can be estimated by generating a Voronoi mesh from the central vein positions. Here, we show a sample 1 cm^2 liver tissue containing 233 hepatic lobules; see Fig. 4

A MATLAB script is included in the github repository (see Appendix D) to implement this algorithm; it has the random seed hard-coded to reproduce the liver tissue in this manuscript.

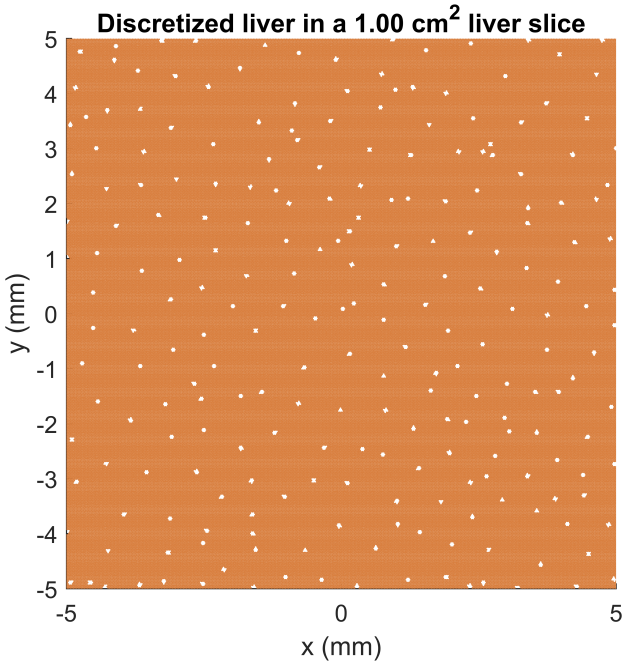

Fig. 4 Synthetic liver tissue dataset: As described in 2.4, a 1 cm^2 generated slice of liver tissue was created. Open regions (white spots) are central veins.

2.5 Creating interactive cloud-hosted PhysiCell models with xml2jupyter

In [72], we introduced *xml2jupyter*, an open source Python package that can map model parameters from PhysiCell's XML configuration file to Jupyter widgets, which can automatically create a Jupyter-based graphical user interface (GUI) for any PhysiCell-based model, including user-friendly widgets to

configure and run the model and visualize results within the notebook. In addition, the Jupyter notebooks and the accompanying simulation executable can be hosted on nanoHUB [73] as a cloud-hosted, interactive version of the simulation model. This facilitates multi-disciplinary communication of the model without need for downloading, compiling, and running the code.

The agent-based model presented in Section 3.9 is available as a nanoHUB app [74] at https://nanohub.org/tools/pc4livermedium. See Fig. 5 for sample screenshots from typical use.

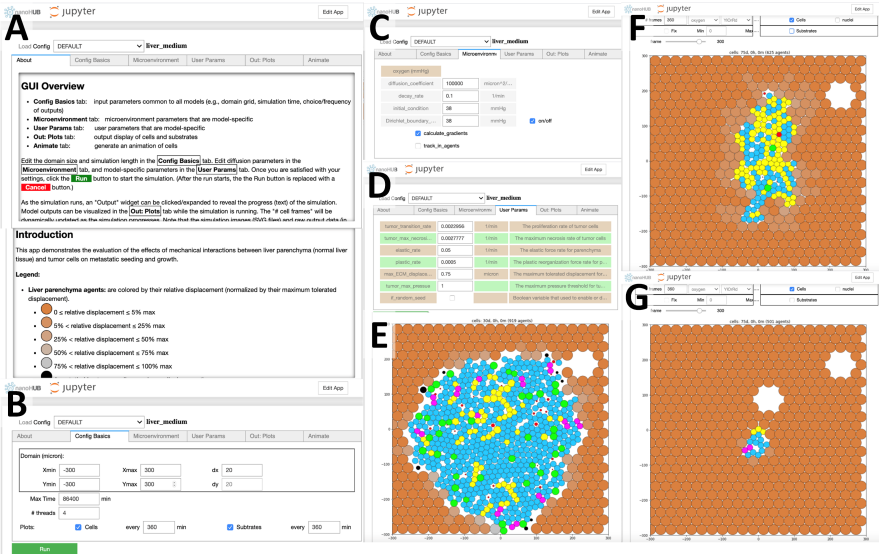

Fig. 5 Cloud-hosted interactive model: Readers can interactively explore the agent-based model at https://nanohub.org/tools/pc4livermedium. (**A**) The *About* tab introduces the model, describes the plot legends, and gives run instructions. Users can modulate the domain size (**B**), diffusion parameters (**C**), and model-specific parameters (**D**). Simulation results can be viewed live in the *Out: Plots* tab, or animated as an mp4 movie in the *Animate* tab. Sample outputs are shown in **E**-**G**.

2.6 Histopathology

Tumor tissues were received from colorectal cancer patients under Institutional Review Board (IRB) approval at the Norris Comprehensive Cancer Center of USC. All subjects gave their informed consent for inclusion before they participated in the study. The study was conducted in accordance with the Declaration of Helsinki, and the protocol was approved by the IRB Ethics Committee of USC (Protocol HS-06-00678; approval date 08-02-2019). The USC Translational Pathology Core processed the formalin-fixed, paraffin embedded (FFPE) tissue biospecimens. Tissue sections were prepared and stained with

hematoxylin and eosin (H&E). The slides were then imaged using the Olympus VS120 Slide Scanner.

3 Results

3.1 Metastatic tumor seeds have little impact on flow in nearby parenchyma, but they increase strain

In the absence of a tumor (control case), our PVE model simulations show that the flow velocity increases in an approximately exponential pattern from the portal vein inlet to the central vein outlet, with velocity magnitudes ranging from 0 to ∼800 μm/sec. The solid matrix strain decreased from approximately 3% at the lobule periphery to 1.7% near the central vein outlet. See Fig. 6.

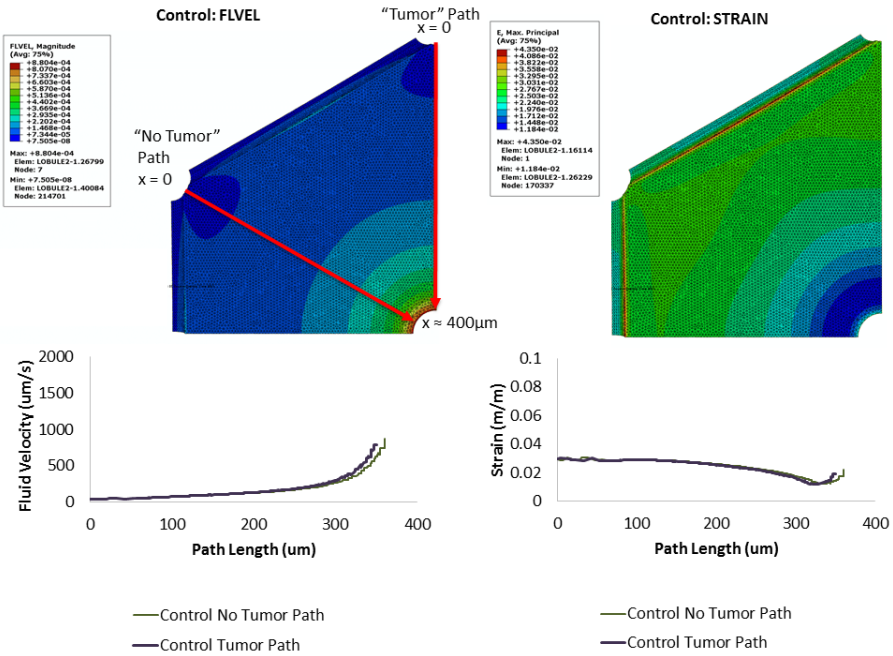

Fig. 6 Hepatic flow: no tumor. The fluid velocity (left plots) and strain (right plots) are plotted across the lobule (top plots) and along "tumor" and "no tumor" paths (bottom plots). Flow accelerates as fluid approaches the central vein, whereas strain slightly decreases.

We next seeded very small micrometastases (50 μm diameter) in the lobule, with no net fluid pressure drop across the tumor boundary. The simulated flow velocity and tissue strain away from the tumor were largely unaffected by the presence of a nearby metastatic seed. See the "no tumor" paths in Fig. 7. Along the "tumor" path, the fluid velocities were notably elevated

in the high permeability tumor condition (200 μm/sec) as compared with the low permeability tumor condition (57 μm/sec) or the normal parenchyme at a comparable location within the lobule (95 μm/sec at 200 μm from the center of the lobule). In both these scenarios, we note that interstitial flow was largely intact near the micrometastasis. (See the top left plot in Fig. 7 for the high-permeability flow profiles, and the lower left plot for the flow profiles along the "tumor" and "non-tumor-paths" for both the high- and low-permeability cases.) The strain increased at the tumor margins, from 3% to $\sim$ 4.2%, and it dropped to negligible values inside the tumor itself as a result of the increased tumor stiffness relative to the surrounding tissue (refer to Supplementary Materials for details regarding tumor stiffness used in the model). See the right plots in Fig. 7.

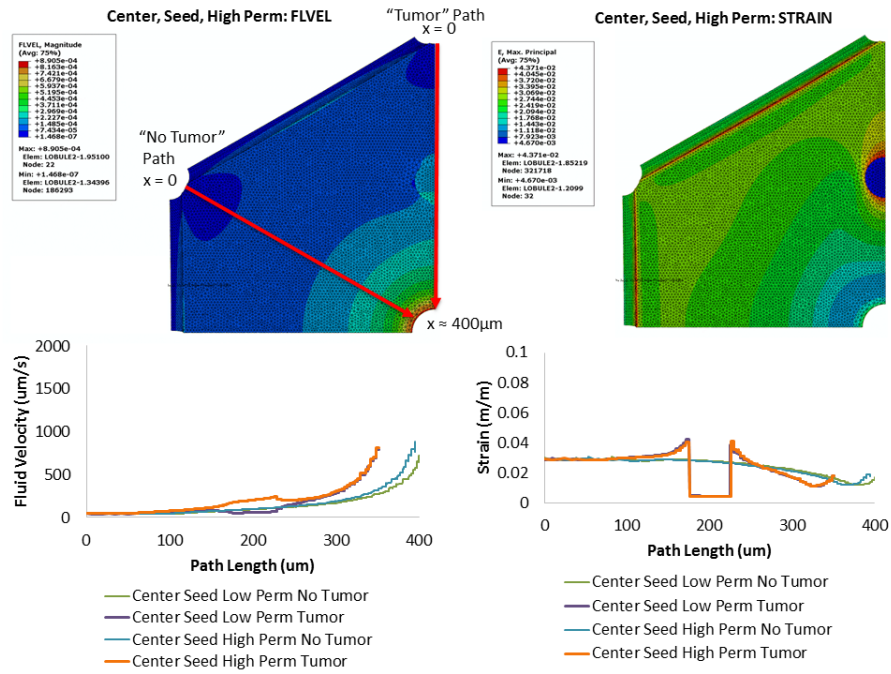

Fig. 7 Hepatic flow: small tumor seeds. A 50 μm micrometastasis is seeded between the portal triad and central vein, with neutral pressure difference at the tumor boundary. The fluid velocity and strain along the non-tumor path are largely unaffected by the nearby tumor, whereas the fluid velocity increases slightly in highly permeable tumors, and decreases in less permeable metastatic seeds (left plots). The tissue strain is very low within the tumor but increases in the parenchyma immediately surrounding the tumor seed (right plots).

3.2 Flow is stagnant within larger micrometastases but not in the surrounding parenchyma

We next simulated the disruption of the liver parenchyma surrounding a 200 μm micrometastasis between a portal vein and the central vein, with the tumor modeled as a pressure sink; see Fig. 8. For the flow path passing through the tumor, the fluid velocity entering the lobule from the portal vein was higher (800 μm/sec) compared with control ($\sim$0 μm/sec), increasing to a maximum of 1370 μm/sec as it approached the tumor boundary. Thus, the flow was non-stagnant in the regions surrounding the micrometastasis. Flow along the path through normal parenchyme had comparable velocities compared to the control near the portal triad and middle of the lobule, but lower velocities towards the central vein outlet. Notably, the fluid velocity dropped to negligible values within the tumor itself.

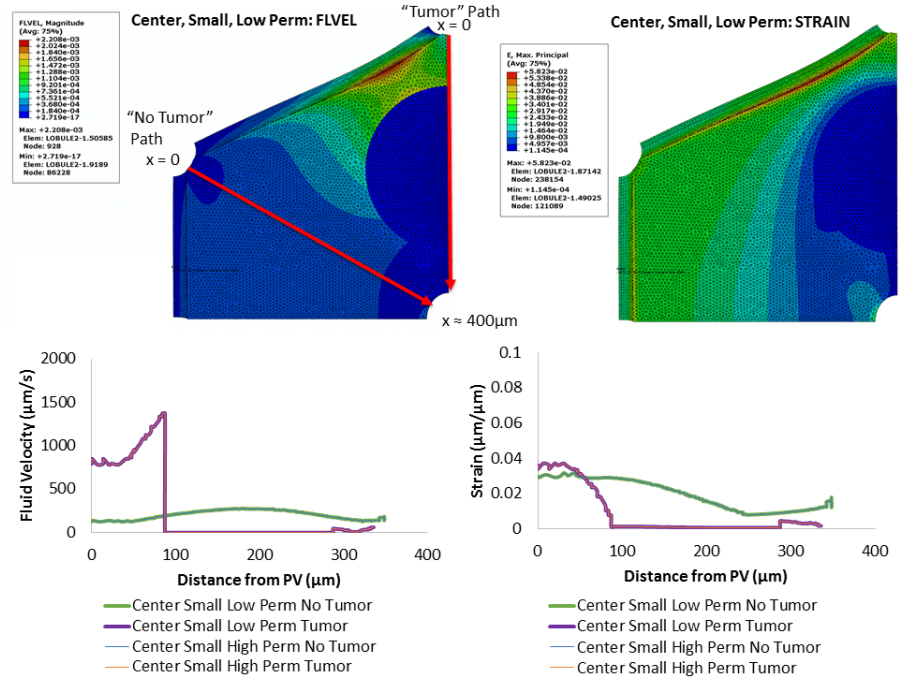

Fig. 8 Hepatic flow: small micrometastasis. A 200-μm micrometastasis disrupts a hepatic lobule, with tumor treated as a net pressure sink. Here, the fluid flow velocity increases "upstream" of the tumor (near portal triad inflow) and decreases near the central vein outlet. The fluid velocity abruptly drops to zero in micrometastases with both high- and low-permeability (left plots).

This trend held for both high and low permeability tumor conditions. Moreover, similar simulations that varied the position and tumor permeability for 200 μm micrometastases similarly showed stagnant flow within the tumors and

non-stagnant (or increased) flow in the regions immediately surrounding the tumors, likely due to the tumor set as a pressure sink (see table in boundary conditions section of supplementary Materials). This was true regardless of the tumor location (center or portal) or permeability (high or low).

This trend continued for larger micrometastases, but with clearer effect. When we placed a 400 μm micrometastasis near a portal vein and treated the tumor as a pressure source, flow was stagnant within the tumor and intact (or accelerated) in the surrounding parenchyma. See Fig. 9. Fluid velocities increased sharply from zero to $\sim$1000 μm/sec at the tumor boundary, then continued to increase up to $\sim$2000 μm/sec at the central vein. Flow along the path through normal parenchyme showed a velocity trend similar to the control condition but with a higher peak velocity ($\sim$2000 μm/sec) at the central vein. This result held for high and low permeability when the tumor was treated as a pressure source (Figs. 9 and S3), or as a net sink (Fig. S6). It also held when the 400 μm micrometastasis was simulated as pressure neutral with low permeability (Fig. S4).

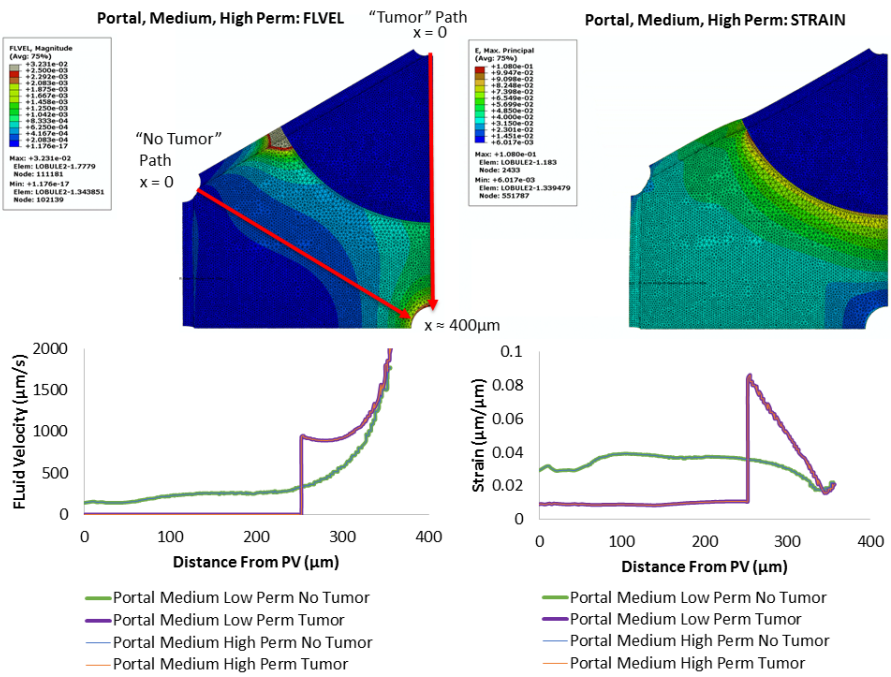

Fig. 9 Hepatic flow: medium micrometastasis. A 400-μm micrometastasis disrupts a hepatic lobule near a portal triad, with tumor treated as a net pressure source. The fluid velocity increases in the parenchyma near the tumor but abruptly drops to zero inside the tumor. There is significant tissue strain in the parenchyma that peaks at the tumor edge and extends significantly into the surrounding tissue before dissipating. These results hold for both high and low tumor tissue permeability, and for neutral tumor pressure (results in supplementary materials.

3.3 Micrometastases can exert tissue strains on the surrounding parenchyma

We observed significant tissue strains in the liver parenchyma surrounding the 400 μm micrometastases (Fig. 9). For the smaller 200 μm micrometastasis, the strain decreased from 3% to zero at the tumor boundary and remained negligible within the tumor itself. For the larger 400 μm micrometastasis, the strains increased sharply at the tumor boundary to a peak value of 9%, the highest strain magnitude of any condition.

We note that setting the tumor as a pressure sink produced a drop in strain at the tumor edge (as in the 200 μm micrometastasis in Fig. 8), unlike the spike in strain noted in the other two conditions (Figs. 7 and 9).

3.4 Biotransport is largely advective and quasi-steady in unobstructed parenchyma; it is largely diffusive within micrometastases

In the PVE simulations, we found that flow was stagnant within most micrometastases, and non-stagnant (e.g., comparable to control or accelerated) within non-obstructed regions of parenchyma. To continue this analysis, let us approximate fluid flow as identical to control conditions outside micrometastases and vanishingly small within tumors.

Using standard conservation of mass laws, we model the transport of a single growth substrate σ (e.g., oxygen or glucose) in liver tissue as

$$\frac{\partial \sigma}{\partial t} = -\nabla \cdot \mathbf{J} - \lambda \sigma \tag{13}$$

$$\mathbf{J} = -D\nabla\sigma + \sigma\mathbf{u}, \tag{14}$$

where $\mathbf{u}$ is the fluid flow field (from the PVE model), λ is the growth substrate consumption rate, D is diffusion coefficient, and with boundary conditions to be described further below.

Based on the typical fluid velocities in unobstructed liver ($||\mathbf{u}|| \sim 10^{-4}$ m/sec) and tumor region ($||\mathbf{u}|| \sim 0$ m/sec), we find (after nondimensionalization) that growth substrate biotransport is largely advective in the parenchyma and diffusive within tumor regions. See Appendix B for expanded detail.

3.5 An analytical approximation to oxygen distribution in unobstructed parenchyma

We can further build on these results to obtain an approximate analytical solution to the quasi-steady substrate distribution within an unobstructed lobule. Because the flow is largely advective-reactive, we can simplify the original equation to

$$\frac{\partial \sigma}{\partial t} = -\nabla \cdot (\sigma\mathbf{u}) - \lambda\sigma. \tag{15}$$

Next, assuming incompressible flow, approximating flow as radially symmetric ($r = 0$ corresponds to the central vein), and matching to the spatial lobule size from the PVE model results, we can obtain an approximate analytical solution for biotransport for oxygen (σ) throughout unobstructed lobules:

$$u(r) = 6 \times 10^4 e^{-0.0075r} \tag{16}$$

$$\sigma(r) = 38.9 e^{0.0223\left(e^{0.0075r}-1\right)}. \tag{17}$$

See Appendix C for expanded mathematical details.

We plot the radial flow and oxygenation profiles for these parameters in a hepatic lobule with radius $R = 400\,\mu$m in Fig. 10; note that $\sigma(R) \approx 60$ mmHg, comparable to the portal venule oxygenation reported in [75].

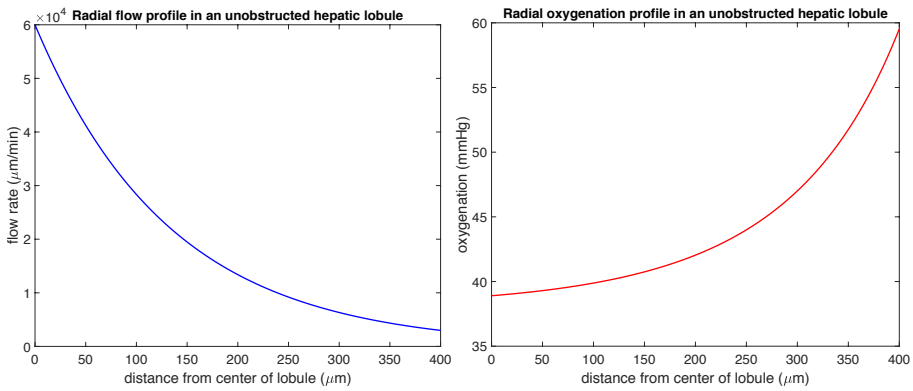

Fig. 10 Approximate analytical solution to flow (**a**) and oxygen distribution (**b**) in an individual, unobstructed lobule

3.6 Approximate oxygen distribution in large tissue sections

We can extend this analytical single-lobule approximation from Section 3.5 to approximate advection-dominated perfusion in a large tissue section. In Section 2.4, we generated a large 1 cm^2 section of liver tissue with hundreds of hepatic lobules with central veins at positions $\{\mathbf{x}_i\}_{i=1}^n$. To approximate the quasi-steady oxygenation pO_2 at any position $\mathbf{x}$ of unobstructed tissue, let us define

$$r(\mathbf{x}) = \min\left\{||\mathbf{x}_i - \mathbf{x}||\right\}_{i=1}^n \tag{18}$$

to be the distance between $\mathbf{x}$ and the nearest central vein. Then we approximate

$$\mathrm{pO}_2(\mathbf{x}) = \sigma\left(r(\mathbf{x})\right). \tag{19}$$

Here, σ is the radial oxygenation profile defined in Equation 17.

Note that this is equivalent to partitioning the 2-D tissue cross-section into a Voronoi mesh (with portal triads at the vertices (representing the flow source) and central veins in the centers) and assuming radial flow within each Voronoi polygon. We show this approximation for the 1 cm^2 tisue in Fig. 11.

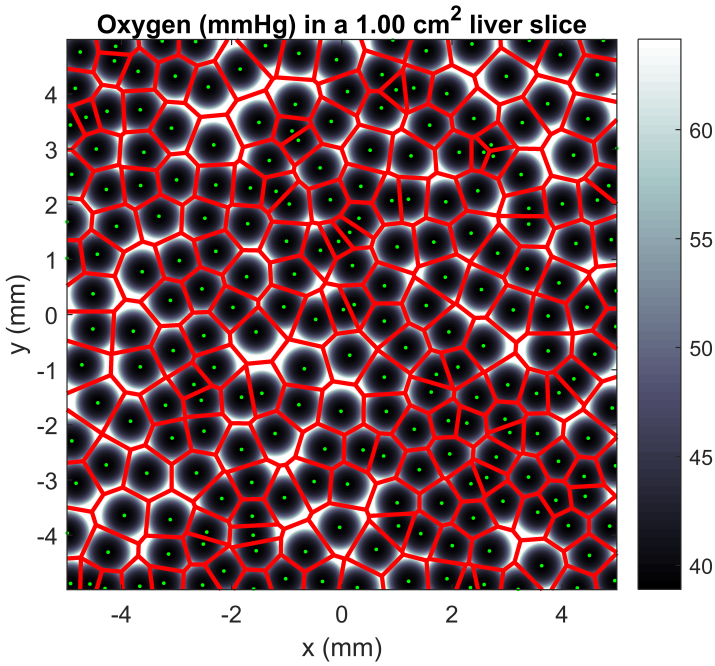

Fig. 11 Approximate oxygen distribution (greyscale values) and Voronoi lobule boundaries (red lines) in a 1 cm^2 liver tissue.

3.7 Millimeter-scale metastases are well-perfused; mechanobiologic growth feedbacks are needed

Many tumor growth models, such as [70, 76, 77] use a diffusing growth factor (e.g., oxygen or glucose) as the main negative feedback on tumor cell proliferation by scaling cell cycling with local substrate availability. As the avascular tumor grows, it consumes and depletes the substrate, thus slowing growth in a negative feedback. See the excellent reveiw in [78]. Because the PVE simulations and subsequent analyses showed that liver parenchyma is well-perfused in tumor-free regions, it raises the question whether substrate-driven growth limits alone can prevent non-physical behaviors (e.g., extensive cell overlap) or if mechanobiologic feedbacks are also required, such as in [79].

To investigate this, we combined the analytical approximation for advection-dominated non-tumor regions from Section 3.6 with the BioFVM diffusion

solver in PhysiCell: in any voxel that does not contain a tumor cell, we assume the tissue has intact flow (as in Section 3.1) and apply the analytical approximation as a Dirichlet node. Prior to tumor seeding, every computational voxel is a Dirichlet node, and so the initial oxygentation matches the profile in Section 3.6. We model any voxel containing tumor cells as permanently disrupted, as suggested by the PVE modeling results. To do this, we permanently remove the Dirichlet node from that voxel and use the usual diffusion solver in BioFVM.

With this methodology, we seeded a 1-cm^2 liver tissue with 10 tumors with a distribution of sizes (diameters) from 250 μm to 2 mm. We then held each tumor static (mechanics, cycling and necrosis disabled) and simulated to steady state. See Fig. 12a. From the heat map of oxygen diffusion (Fig. 12b), oxygen concentration outside of tumors varies from ∼38 mmHg to ∼60 mmHg, while pO_2 inside of tumors depends upon the tumor size. For many of these tumors, most of the tumors were above the hypoxic threshold (5 mmHg; see [69, 70] for more discussion of default parameter values) below which proliferation is disallowed and cells may necrose. The statistics of oxygen distribution in different tumors are shown in (Fig. 12c), with big tumors having lower means and larger standard deviations as a result of the larger oxygen gradients in those larger tumors. In Fig. 12d, we overlay for each tumor its oxygen versus distance from the tumor edge. Note that 800 μm tumor completely lacks a necrotic region ($pO_2 < 5$ mmHg), the 1 mm tumor only has a small region below the threshold, and larger tumors have at least 400-500 μm of viable tissue before reaching the necrotic threshold.

We tested growth of a micrometastasis into liver tissue with oxygen-based growth control (as in [70]) but without a mechanobiologic feedback. We found that pressure peaked at the tumor center and decreased towards the tumor-parenchyma interface, which agrees well with Stylianopoulos et al.'s experimental and mathematical result [80]. See Fig. 13 for an example using the more advanced liver mechanics to be introduced in Section 3.8.2. While liver parenchyma apoptosis near the tumor boundary helped to locally relieve this pressure, we observed an excessive non-physical overlap of cells and (nondimensional) pressures well over 0.5 (the pressure value for a confluent, uncompressed tissue). Therefore, we required a mechanobiologic growth feedback for the tumor cells for metastatic growth in the well-perfused liver environment.

3.8 Modeling tumor-parenchyma mechanobiologic feedbacks

In Sections 3.1-3.3, we saw evidence of significant tumor-parenchyma mechanical coupling, even for static tumors. Moreover, the fast interstitial flow ensures that even moderately large metastases are well perfused, and so diffusion-driven growth limits are insufficient to avoid non-physical model behaviors. We thus incorporated additional biological hypotheses in our agent-based model to account for these effects.

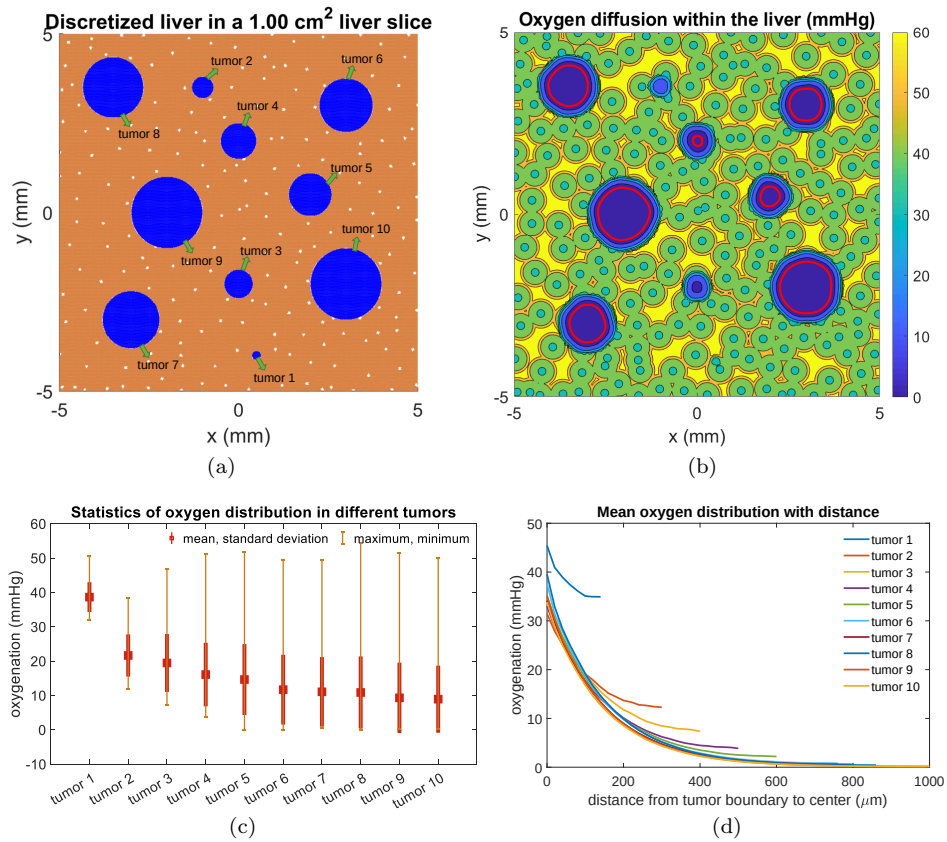

Fig. 12 Oygen distribution inside of 10 tumors (red line is the necrosis threshold value (5 mmHg)) within liver tissue. **(a)**: the 10 tumors in liver tissue; **(b)**: corresponding oxygen map; **(c)**: statistics of oxygen distribution in the different tumors; **(d)**: corresponding mean oxygen distribution with distance

3.8.1 Pressure-regulated tumor cell proliferation

In a form of mechanosensing, cells can sense compression and down-regulate cell cycling to resist overcrowding (e.g., [81, 82]). As inspired by [83] and introduced in [70], cell agents can use their potential functions to construct the local compressive pressure p, which we normalize to 1 for a cell in a densely packed 3-D tissue (12 similarly sized neighbors in dense packing) or 0.5 in 2D (6 similarly sized neighbors in dense packing). We can therefore combine this pressure with the prior oxygen-depenent cycle entry for a mechanosensory cycle arrest:

$$r_{01}(\sigma, p) = \bar{r}_{01}(\sigma) \cdot \min\left\{1,\ \max\left\{\left(\frac{p_2 - p}{p_2 - p_1}\right), 0\right\}\right\} \tag{20}$$

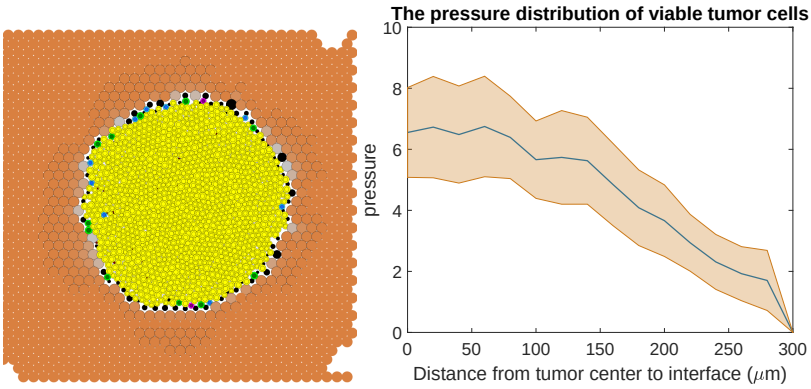

Fig. 13 Micrometastases without a mechanobiologic growth feedback. *Left:* After 10 days of growth, almost all tumor cells have pressure exceeding 1.0, with considerable (non-physical) cell overlap. *Right:* We plot the mean (central curve) and standard deviation (shaded region) of the cell pressure versus distance from the tumor center of mass. Pressure peaks at ~ 7 nearest to the tumor center, gradually decreasing towards zero on the tumor edge where liver parenchyma apoptosis locally relieves the pressure. **Simulation parameters:** r_{E}=0.1 (1/min), r_{P}=0.01 (1/min) and $d_{\max}$=1 μm.

where $\bar{r}_{01}(\sigma)$ is the oxygen-dependent transition rate from the Ki67- phase to the pre-mitotic Ki67+ cycle phase. Assuming that tumor cells can tolerate greater compression than non-malignant cells, we set $p_1 = 0$ and $p_2 = 1$. In this functional form, the "regular" oxygen-dependent cycle entry rate is scaled by the pressure. If $p \geq p_2$, cycling is arrested in the Ki67- phase, and if $p \leq p_1$, then cycling continues without mechanosensory-based restriction.

3.8.2 Elasto-plastic mechanics and mechanosensing in the parenchyma

As noted in Section 2.3.1, we model the parenchyma as a collection of parenchyma agents, rather than modeling at the level of detail of individual hepatocytes and endothelial cells. Each parenchymal agent follows regular adhesion-repulsion mechanics (with a position $\mathbf{x}_i$) based on the standard PhysiCell potential functions [70]. In addition, we model mechanical interactions with the underlying ECM based upon an earlier model we developed in [34].

Each agent i with position $\mathbf{x}_i$ and radius R_i is attached to the ECM at $\mathbf{x}_{i,\mathrm{ECM}}$ and experiences an additional elastic force that resists displacement (deformation) of the cell away from $\mathbf{x}_{i,\mathrm{ECM}}$. Let $\mathbf{d}_i = \mathbf{x}_{i,\mathrm{ECM}} - \mathbf{x}_i$, and let $d_i = ||\mathbf{d}_i|| - R_i$ denote the elastic deformation. Then if r_{E} is a coefficient for the magnitude of an elastic restorative force, then we model (after the "inertialess" balance of force as in [34, 70, 71]) this restorative force an additional term in the cell's velocity:

$$\frac{d}{dt}\mathbf{x}_i(t) = r_{\mathrm{E}} d_i \frac{\mathbf{d}_i}{||\mathbf{d}_i||}. \tag{21}$$

Following [32–34], if a tissue remains in a strained state, it can undergo plastic reorganization. We model this relaxation process by evolving $\mathbf{x}_{i,\mathrm{ECM}}$ towards $\mathbf{x}_i$ with a (slower) relaxation rate parameter r_P:

$$\frac{d}{dt}\mathbf{x}_{i,\mathrm{ECM}} = r_\mathrm{P}\left(\mathbf{x}_i - \mathbf{x}_{i,\mathrm{ECM}}\right) \tag{22}$$

Lastly, we assume that parenchymal agents undergo apoptosis if their deformation (displacement) d_i exceeds a maximum tolerated deformation (d_max). Taken together with Section 3.8:

1. The elasto-plastic parenchyma model allows a growing micrometastasis to strain the liver tissue, potentially to the point of local tissue death. This can free space for the micrometastasis to expand.
2. The elasto-plastic parenchyma model imparts a resistive force on the cells in a growing micrometastasis, which can lead to compression and thus down-regulate cycling to slow the growth of the metastasis.

3.9 Large-scale model exploration and initial observations

We initiated a series of simulations of 90 days of growth from a single seeded metastatic cell in the center of a 0.5 cm × 0.5 cm liver tissue. We selected 27 parameter sets (see Table 2) based on previous experimental [84] and simulation [34] results. In particular, the base parameter set uses $r_\mathrm{E} = 0.1$ min^{-1} so that elastic deformation occurs on the time scale of minutes, $r_\mathrm{P} = 0.001$ min^{-1} so that plastic relaxation is two orders of magnitude slower than the elastic response, and $d_\mathrm{max} = 1.5$ μm is on the order of 10% of the size of a parenchyma agent (15 μm radius). We increased and decreased each of these parameters by a factor of 2, yielding 27 parameters sets, and ran 10 simulations per parameter set due to PhysiCell's stochasticity (a total of 270 simulations).

We saved simulation outputs (SVG images and MultiCellDS simulation snapshots [70, 85]) every 6 hours for each run. The simulations were performed on the Big Red 2 supercomputer at Indiana University. Big Red 2 has 344 XE6 (CPU-only) compute nodes and 676 XK7 "GPU-accelerated" compute nodes, providing a total of 1020 compute nodes, 21,824 processor cores, and 43,648 GB of RAM. Each XE6 node has two AMD Opteron 16-core Abu Dhabi x86-64 CPUs and 64 GB of RAM. Each model was run on a single node using 32 threads. All jobs (270 runs) were submitted as a batch. Each simulation completed in approximately 22 hours, and with a total wall time of approximately of 292 hours.

r_E (min^{-1})	0.05	0.1	0.2
r_P (min^{-1})	0.0005	0.001	0.002
d_max (μm)	0.75	1.5	3

Table 2 Parameters used for the agent-based model biomechanics investigation.

In Fig. 14, we plot the final images (at t = 90 days) for a representative simulation for each parameter set. In these and all subsequent figures, blue cells are Ki67- tumor cells (quiescent), green cells are Ki67+ cells preparing for division, magenta cells are Ki67+ cells following mitosis, red cells are apoptotic, and brown cells are necrotic. Tumor cells with pressure p exceeding the maximum pressure $p_2 = 1$ are colored yellow; these cells will arrest cell cycling in the Ki67- state. Liver parenchyma agents are shaded from brown to bright magenta based upon their displacement (strain) relative to their maximum displacement $d_{\max}$ (brightest magenta cells have the greatest displacement). Parenchyma agents with displacement exceeding 0.01 $d_{\max}$ were given a black outline to further indicate regions of tissue deformation. Apoptotic parenchyma are colored black.

The final tumor size decreases with increasing $d_{\max}$ (maximum tolerated deformation). For $d_{\max} = 3$ μm (Fig. 14c-d), the majority of tumor cells are yellow, indicating high pressures and prevalent cycle arrest. Tissue strain extends far into the surrounding parenchyma. (See bands of parenchyma with outlines in Fig. 14d.) In these conditions, the final tumor are small with irregular morphologies. For lower values of $d_{\max}$, the tumor-parenchyma boundary is much smoother. Tumors exceeding approximately 1 mm in diameter showed necrotic regions.

3.10 Tumor-parenchyma biomechanical interactions generate pressure inside tumors and tissue strains in the nearby parenchyma

For $d_{\max} \leq 1.5$ μm, the greatest concentration of tumor cells exceeding their arrest pressure occur in the outer portion of the viable rim where tumor cell proliferation has the highest probability. As daughter cells are generated and grow, the tumor tissue encounters (elastic) mechanical resistance by the parenchyma, leading to the local pressure increase. (See the yellow cells in Fig. 14a.) In necrotic regions, shrinking necrotic cells locally reduce the pressure; this is reflected in the reduced density of yellow cells near the perinecrotic boundaries. See a cross-sectional plot of the tumor pressure and parenchyma strain (for $r_{\mathrm{E}} = 0.05$ min^{-1}, $r_{\mathrm{P}} = 0.0005$ min^{-1}, and $d_{\max} = 0.75$ μm–a parameter set that permits sustained tumor growth) in Fig. 15.

The proliferative tumor regions expand the volume of the tumor viable rim, thus deforming the nearby parenchyma. The parenchyma strain (brightest magenta: greatest relative deformation) reaches a maximum at the tumor-parenchyma interface and steadily dissipates with distance from the tumor, similarly to the poroviscoelastic simulation results. Apoptosis (black agents) occurs nearest to the tumor-parenchyma interface wherever the parenchyma strain exceeds its maximum tolerance. See Fig. 15.

Fig. 16 plots key properties of tumor and parenchyma versus time (days) with the same parameters as Fig. 15, visualized for all 10 simulation replicates. For the first 20 days, the fraction of the tumor exceeding the maximum pressure steadily grows, reflecting both the proliferation and the mechanical

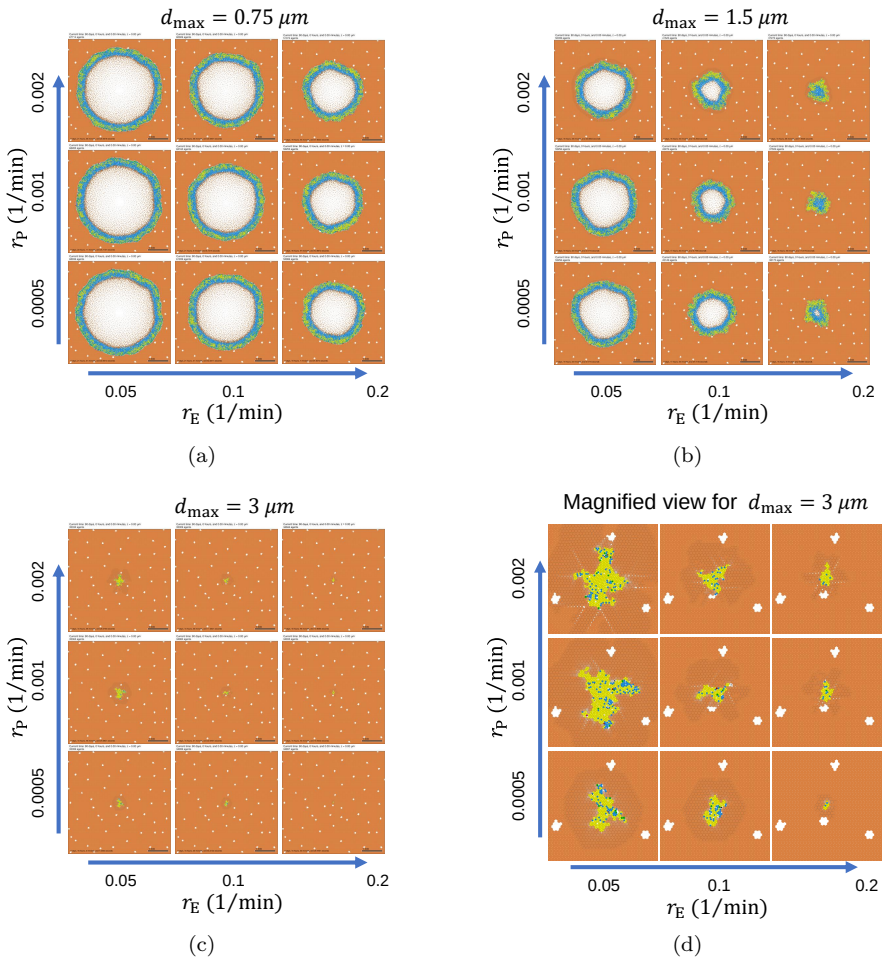

Fig. 14 (a-c): Final tumor shapes at t = 90 days in 0.5 cm × 0.5 cm liver tissue with different biomechanical parameters (r_E: elastic response rate; r_P: plastic relaxation rate; d_{max}: maximum tolerated deformation). **(d):** 5× magnification of the tumors in **(c)**. **Legend:** Tumor cells are shaded blue (Ki67-), green (Ki67+ prior to division), magenta (Ki67+ after division), red (apoptotic), or brown (necrotic). Yellow tumor cells have pressure p exceeding their tolerance and will arrest in the Ki67- state. **Liver parenchyma** is shaded from brown (no deformation) to bright magenta (maximum tolerated deformation), and black parenchyma is apoptotic. Black outlined parenchyma agents have been displaced at least 1% of their maximum tolerated displacement.

resistance of the surrounding parenchyma. Afterwards, the pressure reduces because (1) the pressure feedback reduces proliferation, and (2) necrosis acts as a pressure release. Over time, these effects balance to reach a steady state. See Fig. 16(a-b). The mean tumor pressure behaved similarly (result not shown). The mean parenchyma displacement increases steadily over time(Fig. 16(c),

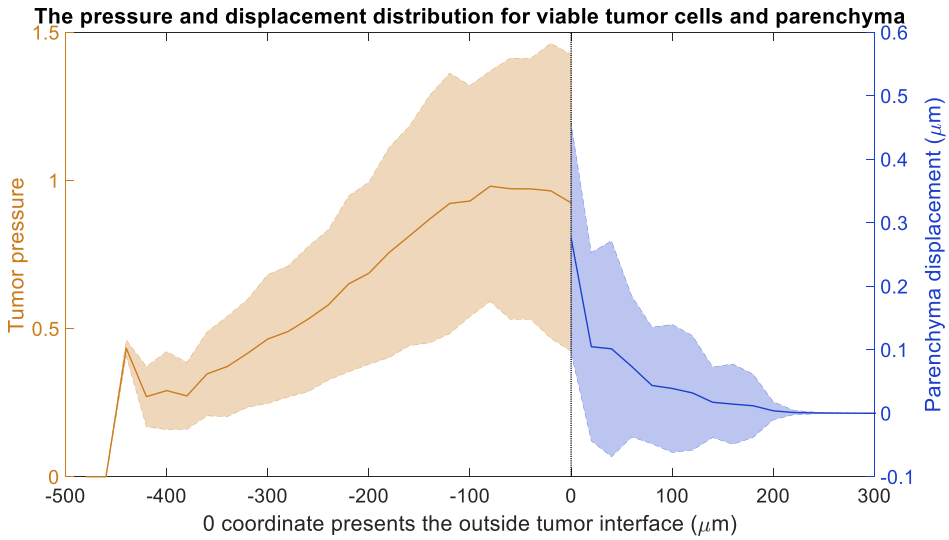

Fig. 15 Pressure distribution of viable tumor cells and the displacement distribution of parenchyma at t = 90 days, where r_{E}=0.05 (1/min), r_{P}=0.0005 (1/min) and $d_{\max}$=0.75 μm. Cells are colored as described in Fig. 14.

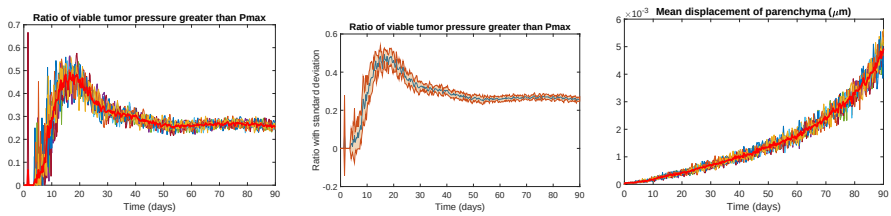

(a) (b) (c)

Fig. 16 Longitudinal changes over 90 days in **(a-b)** the fraction of tumor cells exceeding the arrest threshold, and **(c)** the mean parenchyma displacement. Here, r_{E}=0.05 (1/min), r_{P}=0.0005 (1/min) and $d_{\max}$=0.75 μm.

which reflects the increasing tumor-stroma contact area as the tumor expands into the parenchyma.

3.11 Predicted parenchyma deformations are observed in human colorectal cancer metastases

The model predictions of deformed liver parenchyma can be observed in clinical samples. In Fig. 17, we show a hematoxylin and eosin (H&E) stained whole slide image of human liver tissue with a colorectal cancer metastasis. Regions of compressively strained liver parenchyma (C) are macroscopically observable near the tumor boundary (dashed line), visible as regions of more concentrated eosin staining. See Fig. 17A.

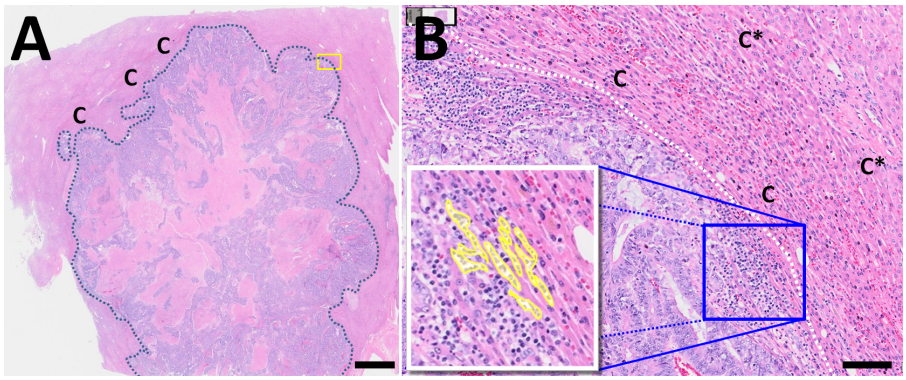

Fig. 17 Colorectal cancer metastasis in human liver: A: Hematoxylin and eosin (H&E) stained whole slide image of a CRC metastasis in liver. Note the deformed liver parenchyma (C) near the tumor-parenchyma boundary (dashed line), which indicates sufficient tissue deformation (strain) to be observed macroscopically. Scale bar: 2 mm. **B:** Magnified view of the yellow box from A near the tumor boundary. Note that the regular liver microstructure has been deformed (strained) to be highly anisotropic, indicating compression in the direction orthogonal to the tumor boundary (dashed line) and potential stretching in the direction parallel to the boundary. This deformation is greatest near the tumor (C) and decreases farther from the tumor boundary (C*). The yellow highlighted cells in the inset show tumor cells growing along paths of mechanical least resistance in collapsed sinusoids. Scale bar: 100 μm.

In a magnified view of the sample (Fig. 17B), we see that the parencyhma nearest to the tumor is highly anisotropic: it has been compressed in the direction parallel to the tumor boundary (in the direction of tumor growth), and stretched in the direction parallel to the boundary. This is consistent with deformation from a growing tumor: compression in the direction of growth, and stretch in the direction parallel to the interface. Moreover, just as in the simulations, the greatest parenchyma deformation happens nearest to the tumor (annotated as C), and the deformation extends out into the tissue with decreasing effect (C*).

3.12 Metastases can invade along paths of mechanical least resistance

In the simulation results, if the parenchyma was more tolerant of deformation (higher values of $d_{\max}$) but readily deformable (lower r_{E}), then a sufficient amount of parenchyma could be displaced to encapsulate the tumor. Plastic reorganization (represented by r_{P}) results in a decreasing elastic force, which in turn slowly relieves the pressure on the tumor cells to allow sporadic proliferation. Continued tumor proliferation into this tough yet well-perfused tissue lead to local "fingering" morphologic instabilities, generally nucleated along paths of mechanical least resistance (e.g., in gaps between parenchyma agents). See Fig. 18. We note that this is consistent with prior predictions made with continuum methods, where fingering morphologic instabilities were

observed in growth into stiff, well-perfused tisues [76]. Note that this is also observed in clinical tissues: Fig. 17B shows tumor cells growing in collapsed liver sinusoids–paths of mechanical least resistance (see the yellow highlighted regions in the figure inset).

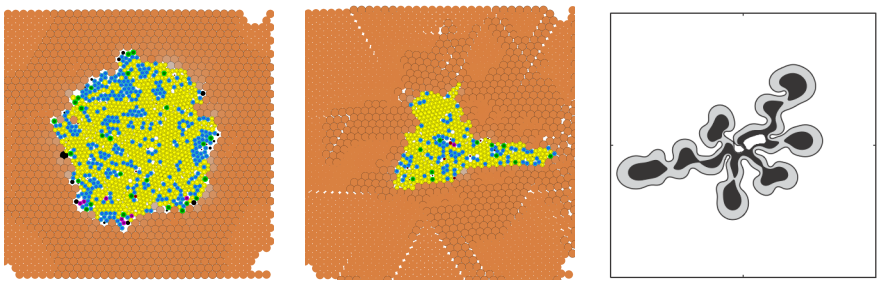

(a) r_E=0.1, r_P=0.01, d_{max}=1 (b) r_E=0.1, r_P=0.01, d_{max}=3 (c) continuum methods [76]

Fig. 18 Fingering metastatic growth: (a)-(b): Growth into initially compliant parenchyma that tolerates deformation can lead to fingering morphologic instabilities, where tumor growth invades along directions of mechanical least resistance. Cells are colored as described in Fig. 14. **(c):** Macklin and Lowengrub previously used continuum methods to predict that tumor growth into relatively stiff, well-perfused tissue can lead to fingering-shaped morphological instabilities [76]. See Fig. 17 for an example of CRC growth along paths of mechanical least resistance (yellow highlighted regions in the blue inset box).

3.13 Micrometastases may remain dormant in highly elastic parenchyma

When the parenchyma was more tolerant of deformation (higher values of d_{max}), but readily deformable (lower r_E) with slower plastic reorganization (lower values of r_P), then the tumor becomes encapsulated as in Section 3.12. With slower plastic relaxation of the parenchyma, however, the elastic force (and hence the high tumor mechanical pressure) is sustained, leading to tumor dormancy. See Fig. 19. The results show that some rigid tissue regimes can arrest the growth of micrometastases, which also agrees with the experimental observations that solid stress can inhibit the growth of multicellular tumor spheroids [37, 80, 86].

3.14 Changes in parenchyma biomechanics can trigger "reawakening" of dormant micrometastases

To investigate the impact of a change in parenchyma tissue biomechanics (e.g., after an acute injury or illness that drives tissue remodeling, or during aging),

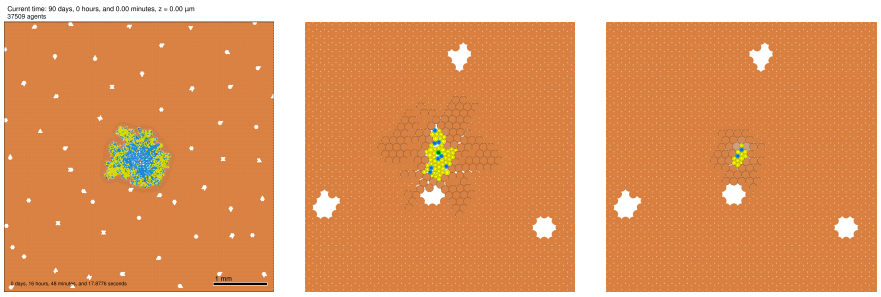

(a) r_E=0.2, r_P=0.001, d_{max}=1.5 (a) r_E=0.2, r_P=0.001, d_{max}=3 (b) r_E=0.2, r_P=0.0005, d_{max}=3

Fig. 19 Dormant micrometastases: Metastatic growth into highly elastic parenchyma with high tolerance for deformation can lead to tumor encapsulation. If plastic relaxation is slow, mechanical feedbacks are sustained, leading to slow (but potentially invasive) growth (a) or tumor dormancy (b-c). Cells are colored as described in Fig. 14.

we first simulated three tumors for 90 days until reaching dormancy as described in Section 3.13 ($r_E = 0.2$ min^{-1}, $r_P =$ min^{-1}, $d_{max} = 3\,\mu$m). We then simulated an additional 90 days of growth under three scenarios: (I: *control*) left the parameters unchanged (top row in Fig. 20); (II: *increased deformability*) reduced r_E to 0.05 min^{-1} (middle row in Fig. 20); and (III: *reduced tolerance to deformation*) reduced d_{max} to 1.5 μm (bottom row in Fig. 20).

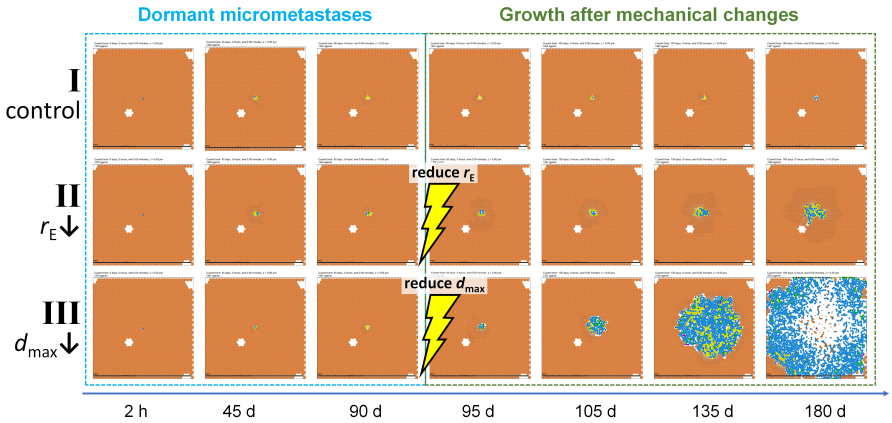

Fig. 20 Dormant tumor reawakening after biomechanical changes: Three micrometastases were grown to dormancy over 90 days in identical conditions and then subjected to biomechanical changes in the liver parenchyma before an additional 90 days of growth. Tumor I (control) remained dormant for the extra 90 days. Tumor II (r_E) "reawakened" with slow growth. Tumor III (reduced tolerance to deformation d_{max}) reawakened to exhibit rapid growth. Cells are colored as described in Fig. 14.

With no changes in the parenchyma (tumor I in Fig. 20), the tumor remained dormant for an additional 90 days. Reducing the elastic parameter r_{E} as in tumor II in Fig. 20 allowed the surrounding parenchyme to more easily deform by decreasing the elastic force resisting tumor growth. Under these conditions, the dormant tumor "reawakened" to slow, invasive growth. Reducing the parencyma's tolerance for deformation $d_{\max}$ as in tumor III in Fig. 20 resulted in faster liver tissue death, allowing the tumor to more easily displace and replace it. In these conditions, the dormant tumor reawakened to rapidly grow through the tissue.

4 Discussion

Liver metastases represent the final stage for many types of cancer, with limited clinical options to offset patient mortality. Yet the biomechanical interactions that favor metastases to seed in liver tissue and the conditions that enhance their growth remain poorly understood. This study presents a modeling framework to systematically evaluate the effects of mechanical interactions between liver parenchyma and tumor cells on metastatic seeding and growth. The biomechanics of centimeter-scale liver tissue are simulated by coupling a poroviscoelastic (PVE) model with an agent-based model (ABM).

4.1 Fluid flow and effect on tissue strain

The results show that changes in tumor permeability may have little to no effect when the tumor is modeled as a pressure source (Fig. 9) or sink (Fig. 8). However, when the tumor is modeled as neutral (neither source nor sink, Fig. 7), fluid flows faster through high permeability tumor tissue and slower through low permeability tissue as compared with normal parenchyma. For the neutral condition, high tumor permeability is also associated with higher tumor stresses (Supplemental Information). When the tumor is modeled as a pressure sink (Fig. 8), most of the fluid entering the lobule drains through the tumor boundary, so that fluid velocities in central vein regions are negligible. Setting the tumor as a pressure sink also produces a drop in stress and strain at the tumor edge, unlike the spike in stress and strain noted with the other two conditions. Lastly, modeling the tumor as a pressure source produces the highest overall magnitudes of fluid velocity and strain (Fig. 9). The ABM results show that tumors reached smaller sizes when growing in liver tissues that could tolerate large deformations (larged values of $d_{\max}$) due to stress-induced apoptosis for parenchyma, discussed in Section 3.8.2. The parenchyma agents imposed larger elastic forces on tumor cells, resulting in mechanobiologic growth arrest, even with readily available oxygen and nutrients.

4.2 Scaling up to large tissue

The results overall support the notion that while biotransport is largely advective and quasi-steady in unobstructed parenchyma, it is largely diffusive within micrometastases. We further implemented an analytical single-lobule approximation to simulate advection-dominated perfusion in a large tissue section, along with mechanobiologic growth feedback for the tumor cells for metastatic growth in the well-perfused liver environment. This enabled the evaluation of pressure-regulated tumor cell proliferation and the simulation of elasto-plastic mechanics and mechanosensing in the parenchyma. A large-scale model exploration shows that tumor-parenchyma biomechanical interactions generate pressure inside tumors and tissue strains in the nearby parenchyma. The model predictions of deformed liver parenchyma around tumor boundaries can be observed in clinical samples colon cancer liver metastases.

4.3 Micrometastatic dormancy and growth

Overall, the modeling framework presented here provides a platform to explore the mechanobiological conditions that lead to metastatic seeding, dormancy, and growth in liver tissue [87]. The simulation results show that micrometastases may remain dormant in highly elastic parenchyma. These results are consistent with observations using a 3D ex *vivo* hepatic microphysiological system, showing that the proportion of MDA-MB-231 breast cancer cells entering dormancy increased significantly when in a softer (more deformable) hydrogel-supported tissue compared to a stiffer polystyrene scaffold [88]. Changes in parenchyma biomechanics can trigger "reawakening" of dormant micrometastases, with metastatic growth representing an invasion along paths of mechanical least resistance. In particular, changes in liver tissue deformability could occur when injury or aging damages the structural integrity of extracellular matrix, such as by degradation of collagen and elastin or decreased cross-linking [5, 89, 90].

4.4 Liver injury promotes metastatic growth

A decrease in the overall resiliency of hepatocytes due to injury or illness may additionally lead to liver tissue changes favoring metastatic growth. For example, aging as well as fatty liver disease are known to reduce the regenerative capacity of the liver parenchyma [89]. Illness or injuries that compromise non-parenchymal cells (e.g., Kupffer cells, leukocytes, or sinusoidal endothelial cells) could potentially contribute to both of these scenarios [89]. In [56], a microphysiologic system was used to study breast cancer metastasis in liver tissue, finding that for particular cells (MDA-MB-231), the presence of intact non-parenchymal cells was associated with increases in cancer attenuation signals and decreases in pro-inflammatory signals.

Several hallmarks of cancer in the liver, such as angiogenesis, altered proliferation, and apoptosis have been hypothesized to be mediated by alterations in signaling between integrin receptors and the ECM [91]. It has been shown that liver injury, primarily in the form of fibrosis, promotes cell adhesion to the hepatic ECM, thus potentially favoring cancer cell metastatic seeding. Using data from liver exposed to chronic carbon tetrachloride (CCl4) to induce fibrotic scarring in a mouse model, integrin receptor divalence and clustering were mathematically modeled to predict an increase in integrin binding for several receptors for which signaling is known to increase following CCl4 exposure [41]. In particular, the immune response to liver injury is known to affect in situ cancer progression. These effects are poorly understood and deserve further study. With data from experiments to determine ECM density and macrophage-associated cytokine levels, the effects of ECM remodeling and macrophage polarization on liver tumor growth were recently evaluated via computational modeling. The simulations indicated that even in a highly vascularized microenvironment as exists in the liver, metastatic tumor growth could be decreased compared to less vascularized primary tumors due to high local M1 macrophage-induced cytotoxicity [43].

4.5 Aging promotes ECM changes favoring metastases

It is well known that aging-associated cellular and molecular changes in non-cancerous cells can contribute to a microenvironment favoring tumor progression, including biophysical changes to the ECM [90]. In particular, mechanical alterations including strain-stiffening, increased cross-linking, and fiber realignment are thought to be critical in promoting cancer growth and invasiveness [92, 93]. Further, ECM stiffening and remodeling is promoted by the secretion of factors from stromal components that become senescent with age [94]. In turn, the ECM changes affect the immune system response [95]. Interestingly, while aging can lead to increased local tissue stiffness and fibrosis, dysregulation of ECM constituents crosslinking can also yield loose, disorganized fragmented collagen [5]. These changes facilitate mechanically weak tissues, which can promote tumor invasion. Thus, aging can lead to both tissue stiffening and softening, which in their own ways facilitate tumor progression and invasiveness.

These biological observations are recapitulated by the simulation results of this study. The effect of tumors growing to a steady size due to mechanical feedback (Fig. 14) realistically relates to tumor dormancy. Once injury or aging mechanically weaken the liver tissue, dormant micrometastases could resume growth. If the mechanical changes result in fibrosis that leads to local tissue stiffening, which upon plastic reorganization of the ECM is projected by the model to induce a “fingering” tumor invasion pattern to circumvent the mechanical constraints (Fig. 18).

Our results showing ECM-induced mechanical restraint on tumor cells are consistent with findings by [96], who performed experiments to evaluate the

effect of collagen matrix remodeling in aging skin on melanoma metastasis and immune response. A mathematical model was implemented to evaluate the effect of inter-fiber crosslinks on the deformation of collagenous ECMs and the two-way interactions between the strain-stiffening behavior of fibrous ECM and cellular contractility. The simulations showed that HAPLN1, the most abundantly secreted ECM constituent by fibroblasts, significantly alters matrix organization and inhibits cell motility [96]. Related to these interactions, a mechanochemical free-energy-based method was recently developed to elucidate the two-way feedback loop between stress-dependent cell contractility and matrix fiber realignment and strain stiffening [97], validated by analyzing the invasion of melanoma cells in collagen matrix of different concentration. The model was able to find a critical stiffness (EM=0.15 kPa) required by the matrix to break intercellular adhesions and initiate cell invasion. Below this critical stiffness, spheroids kept stable as driving forces could not overcame cell adhesion, while the driving force could break the adhesions and induce invasion when the stiffness was beyond the critical value. In addition, it was found that enhancing collagen concentration in the ECM increased the density of the cell-adhesive ligands, which also in return promoted cell invasion [97].

4.6 Study limitations

The modeling framework presented here has several limitations, as only a subset of key biology is represented. The integration of additional biological details is expected to refine the results and potentially lead to further insights. For example, the incorporation of additional key cell types related to metastatic inception and progression such as fibroblasts and immune cells would provide for the simulation of enhanced cell-cell and cell-matrix interactions. Potentially, the model could be enhanced to simulate signaling traffic between cells and the matrix, scaling down to the integrin level. The structure of the liver could be more detailed, e.g., refining the microstructure of sinusoids to more faithfully represent the organ structure.

In spite of these limitations, the current framework shows that the synergistic integration of multiple modeling approaches may provide insight into cancer behavior. In particular, the model enables evaluating the impact of metastases on perfusion flow, the accumulation of stresses and strains in the local parenchyma, and how these effects altogether support the notion that biomechanical interactions between metastatic tumors and their microenvironment have a role in cancer behavior. Although previous work has investigated molecular-scale feedback mechanisms (e.g., inflammation and other cross-signaling), few studies have focused on purely mechanical feedbacks. Our results suggest that conditions exist for which mechanical feedback alone could explain observations of metastatic progression in the liver, which should reinforce previously studied bioechemical feedbacks. Further, the discrete model formulation presented herein was able to recreate continuum-level pressure and mechanics conditions with relatively simple cell rules, compared to more

complex continuum-scale formulations (e.g., Cahn-Hilliard based models) [78]. This relative simplicity offers the promise of easier translation of experimental observations to model cellular agent hypotheses to observe macro-scale effects.

4.7 Future directions

The proposed modeling framework enables evaluation of biomechanical interactions (adhesive, repulsive, and elastic forces on short time scales, and plastic reorganization on longer time scales) on metastatic tumor cell seeding and growth in liver tissue. The simulation results indicate that there exist conditions for which these interactions may arrest micrometastatic growth and prevent newly arriving cancer cells from establishing new foci. Future work will examine in more detail the role of tissue microstructure, such as sinusoids, on metastatic progression. In particular, colorerectal cancer metastases create glandular structures that are not fully solid. The associated microlumens could provide some stress relief and allow cell tumor and parenchymal cells to intermix, rather than undergo more homogenous compression. An improved understanding of these as well other tumor structural characteristics when interacting with liver tissue could eventually lead to patient tumor-specific therapy to prevent and reverse metastatic seeding and progression.

Acknowledgements The authors acknowledge funding by National Science Foundation (YW, PM: 1720625), the Breast Cancer Research Foundation (PM), the Jayne Koskinas Ted Giovanis Foundation for Health and Policy (PM), the National Cancer Institute (EB, KN, HBF, SM, JLS, PM: 1R01CA180149; SM, PM: 1U01CA232137). We would like to acknowledge the Miami Redhawk Cluster and the Ohio Supercomputer Center for access to computing resources to complete this work. We would also like to thank Dr. Jens Mueller of the Miami University Research Computing Center for assistance with Abaqus model development. The authors gratefully acknowledge access to FutureSystems at the Digital Science Center, Luddy School of Informatics, Computing, and Engineering, and to the Big Red II supercomputer at Indiana University, Bloomington. We would like to thank the USC Translational Pathology Core and Roy Lau (USC) for assistance with patient tissue processing, staining, and imaging. We thank Randy Heiland (IU) for support in creating and refining the nanoHUB liver app. We thank John Metzcar (IU) for helpful comments on the manuscript.

A Expanded modeling review

Here, we give an expanded review of prior mathematical modeling in liver biology, liver metastases, and cancer mechanobiology.

A.1 Liver regeneration

Hoehme et al. used a closed source agent-based modeling (ABM) framework similar to PhysiCell [70] to model liver damage and evaluate the cell-scale hypotheses needed for successful regeneration of the microarchitecture [19]. The model successfully replicated all hepatocytes and sinusoids within a liver lobule during regeneration [19]. More recently,

they used a deformable cell-based model to explore how liver lobule cells regenerate with mechanical stress effects [20], finding that the migration forces that a cell needs to exert on its environment are much smaller than those predicted by center-based models that do not explicitly model cell morphologies. (Center-based models are off-lattice methods that track each cell's center of mass and size, typically using one agent to represent one cell [98]).

A.2 Liver toxicology

Schwen et al. described a methodology of exploring whole-body pharmacokinetics models based on a liver model, integrating from cells through sinusoids and the organ to the whole organism [23]. Sluka et al. developed a multi-scale, liver-centric physiologic-based pharmacokinetics (PBPK) model to study acetaminophen pharmacology and metabolism [24]. They explored drug uptake and transport at the whole body level, blood flow at the tissue/organ level, and metabolism at the sub-cellular level, showing the model is capable of predicting liver toxicity from acetaminophen overdose.

A.3 Interstitial flow and mechanics in liver tissues

Rani et al. presented a computational fluid dynamics (CFD) model of non-Newtonian blood flow within a portal vein, hepatic artery and two sinusoids [25]. Ricken et al. developed a two-scale, continuum multicomponent model for studying blood perfusion and cell metabolism within the liver [28]. They used porous media theory to explore perfusion within lobules, with a focus on advective and diffusive solute transport. Lettmann et al. used a porous-medium method to simulate the microcirculation fields of liver lobules [26]. They captured the blood flow velocity inside the sinusoids and oxygen consumption of Rappaport's liver acinus model. The work found that the liver microcirculation plays an important role in establishing inflammatory cytokine levels.

White et al. presented a convection-diffusion-reaction partial differential equation (PDE) model that coupled blood flow, drug distribution, and clearance in a 3-D liver [29]. Siggers et al. presented a mathematical model that considers the sinusoidal and interstitial spaces as porous media to simulate the blood, interstitial flow and lymph production in the liver [27]. Meyer et al. developed a 3D multi-scale model that explored the biliary fluid dynamics in the mouse liver lobule, predicting gradients of bile velocity and pressure within the lobule [31]. They found that osmotic effects and bile canaliculi contractility result in the bile flow. The multi-scale model is capable of predicting the biliary distribution on drug-induced liver injury. Nishii et al. developed sophisticated poro-viscoelastic (PVE) models that extend porous flow models (as described above) by coupling the flow to a moving, viscoelastic tissue [30]. We shall describe this model further below.

A.4 Tissue mechanics in tumor growth

Ambrosi et al. developed an elasto-visco-plastic model that used phase field methods to describe the mechanical stress of tumor cell suspensions and aggregates [32, 33]. The model illustrates tumor growth responses to mechanical stress, cellular release of stresses, the formation of tumor capsules, and compression of neighboring tissues. Antonio et al. introduced an agent-based model for studying elasto-plastic mechanical interactions between cell-basement membrane (BM)-extracellular matrix (ECM) [34]. Cell motion was modeled as resulting from a balance between adhesive, elastic, and repulsive forces. Over short times, elastic forces were used to simulate the interaction between BM and ECM; over long times, the BM underwent plastic relaxation in response to prolonged strains. Liedekerke et al. used an agent-based model to study the tumor spheroids' growth dynamics in mechanical stress environment with calibrated parameters from experiments [35]. They discovered that the

growth response of cell populations on external mechanical stress is predicable with a same growth progression function.

A.5 Liver metastases in connection with ECM remodeling

Mathematical modeling has also been used to study liver fibrosis [21, 22], while others have used PDE methods to model the growth of liver metastases [38–40]. The kinetics of integrin receptor binding to hepatic ECM proteins following liver injury were recently modeled by Hudson et al. [41]. In follow-on work, the growth of liver metastases was evaluated in a tissue-scale model [43], taking into consideration heterogeneous macrophage populations [42]. ECM from both injured and normal liver was modeled, and parameters were set with values from mouse *in vivo* experiments designed to mimic human tissue conditions.

A.6 Mechanosensing and cancer cell proliferation

Others have evaluated the impact of stress on tumor growth and invasion. Voutouri et al. used both in *vivo* experiment and continuum modeling to study the effect of tumor-host mechanical interactions on the growth of solid tumors [37]. The results show that solid stresses can inhibit tumor cell proliferation, induce apoptosis in surrounding tissue, and lead the surrounding tissue to resist tumor expansion. Cheng et al. [36] built an experimental model to explore spatial distribution of compressive stress around tumor spheroids representing avascular nodules, showing that high mechanical stress results in suppression of tumor cell proliferation and apoptotic cell death.

A.7 Metastasis

While there has been substantial work in modeling primary tumor growth in detailed tissues [98, 99], to our knowledge there has been little work in spatial models of early metastatic seeding and growth under mechanical and flow constraints, especially in liver tissue. Macklin and Lowengrub used a level set / moving boundary method to model tumor growth in simulated brain tissue in [77], but they did not consider mechanobiologic feedback or the impact of flow. Their continuum approach was also not suited to tumors with low cell-cell adhesion or high cellular heterogeneity. Baratchart et al. recently developed a similar model (also based on a porous flow formulation, but without the level set-based sharp interface model) to simulate the merger of renal metastatic foci [100], with a very simple pressure-based tumor cell proliferation rate, and without considering any mechanobiologic feedback in the surrounding normal tissue.

Others have developed network models of metastatic seeding [49–54], but without spatially-resolved simulation of the individual metastasis sites, nor of any mechanical effects. Treatment of liver metastases via nanotherapy taking into account immune system interactions have been recently modeled [44–46], but without considering mechanical effects. In particular, detection and drug delivery to colorectal cancer liver metastases via nanoparticles were simulated in a tissue-scale model in [47, 48]. See [101] for further excellent materials on experimental and mathematical modeling of metastasis.

B Expanded dimensional analysis

Here, we give expanded details on the dimensional analysis needed for Section 3.4.

To evaluate the relative contribution of the advective and diffusive effects in liver interstitial fluid flow, we can rewrite Equations 13-14 as

$$\frac{\partial \sigma}{\partial t} = D\nabla^2\sigma - \mathbf{u}\cdot\nabla\sigma - \sigma\nabla\cdot\mathbf{u} - \lambda\sigma. \tag{23}$$

Approximating the flow field as slowly varying ($\mathbf{u} \approx u\mathbf{w}$ for some constant u and a constant unit vector $\mathbf{w}$), $\nabla\cdot\mathbf{u} \approx 0$. If we nondimensionalize space with scale L and time with scale $\bar{t}$, then this becomes

$$\frac{\partial \sigma}{\partial t} = \left(\frac{D\bar{t}}{L^2}\right)\nabla^2\sigma - \left(\frac{u\bar{t}}{L}\right)\mathbf{w}\cdot\nabla\sigma - (\lambda\bar{t})\,\sigma. \tag{24}$$

Choosing

$$\frac{u\bar{t}}{L} = 1 \text{ and } \lambda\bar{t} = 1 \Longrightarrow \bar{t} = \frac{1}{\lambda} \text{ and } L = \frac{u}{\lambda}, \tag{25}$$

then the nondimensionalized equation becomes

$$\frac{\partial \sigma}{\partial t} = \left(\frac{D\lambda}{u^2}\right)\nabla^2\sigma - \mathbf{w}\cdot\nabla\sigma - \sigma. \tag{26}$$

By prior work [69], $D \sim 10^5 \mu\text{m}^2/\text{min}$ and $\lambda \sim 10\ \text{min}^{-1}$. By the PVE simulations in Section 3.1 and [30], $u \sim 10^{-4}\text{m/sec} = 6\times10^3\mu\text{m/min}$ in the unobstructed liver parenchyma, and so $L \sim 600\ \mu\text{m}$, and $\bar{t} \sim 6$ sec. The diffusion term has relative order of magnitude

$$\frac{D\lambda}{u^2} \sim \frac{1}{36} \approx 0.03. \tag{27}$$

Thus, in unobstructed regions of liver lobule, flow is primarily advective-reactive, and the original equation can be simplified to

$$\frac{\partial \sigma}{\partial t} = -\nabla\cdot(\sigma\mathbf{u}) - \lambda\sigma. \tag{28}$$

Because the time scale is on the order of seconds, advective flow is at quasi-steady state in regions of unobstructed flow when considered on time scales of mechanics (minutes) and tumor growth (hours to days).

Because $\mathbf{u} \sim \mathbf{0}$ inside micrometastases, we find that biotransport in those regions satisfies

$$\frac{\partial \sigma}{\partial t} \approx D\nabla^2\sigma - \lambda\sigma. \tag{29}$$

That is, biotransport is largely diffusive-reactive within tumors.

C Expanded mathematical detail on the radial biotransport approximation

Here, we give expanded mathematical detail on the approximate analytical solutions for oxygen distribution in unobstructed liver tissue, as first introduced in Section 3.5.

Assuming incompressible flow ($\nabla\cdot\mathbf{u} = 0$) and that flow within the lobule can be approximated as radially symmetric ($\mathbf{u} \approx -u(r)\hat{\mathbf{r}}$, where r is the distance from the middle of the central vein), we have

$$\frac{\partial \sigma}{\partial t} = u(r)\nabla\sigma\cdot\hat{\mathbf{r}} - \lambda\sigma \tag{30}$$

$$= u(r)\frac{\partial \sigma}{\partial r} - \lambda\sigma. \tag{31}$$

Under quasi-steady conditions, $\sigma = \sigma(r)$, and we have

$$0 = \sigma'(r) - \frac{\lambda}{u(r)}\sigma, \tag{32}$$

whose analytical solution is given by

$$\sigma(r) = ce^{\lambda \int_0^r \frac{1}{u(s)} ds} \tag{33}$$

for some constant c.

For simplicity, we will approximate the flow profiles in Section 3.1 with the form

$$u(r) \approx ae^{-br} \tag{34}$$

for constants a and b. Notice that $u(0) = a$ and $u(R) = ae^{-bR} = u(0)e^{-bR}$, whereby

$$b = -\frac{\ln\left(\frac{u(R)}{u(0)}\right)}{R}. \tag{35}$$

For consistency with the PVE model, we set $R = 400\ \mu$m.

For this simplified form, we have

$$\sigma(r) \approx ce^{\frac{\lambda}{ab}\left(e^{br}-1\right)}. \tag{36}$$

By the PVE simulations in Section 3.1, we see that $\frac{u(R)}{u(0)}$ is on the order of 0.01 to 0.1, so we choose 0.05. Thus, $b \sim 0.0075\ \mu\text{m}^{-1}$ by Equation 35. Moreover, $u(0) = a \sim 10^{-3}$ m/sec $= 6 \times 10^4\ \mu$m/min. [75] report that liver oxygenation is approximately 38.9 mmHg in central venules, 48.2 mmHg in sinusoids, and 59.8 mmHg in portal venules. So, we set $\sigma(0) = 38.9$ mmHg:

D Code availability

D.1 Poroviscoelastic model

The project files for the poroviscoelastic simulation work are available as open source under the MIT license at

https://github.com/MathCancer/PVE-liver-mets

Zenodo archives

1.0.0 Version used for the PVE simulation studies
https://doi.org/10.5281/zenodo.3779512

D.2 Agent-based model

The core agent-based model (minus the cloud-hosted interface; see Section D.3) is available as open source under the 3-clause BSD license at

https://github.com/MathCancer/liver-mechanobiology

Zenodo archives

1.0.0 Version used for the main parameter studies
https://doi.org/10.5281/zenodo.3766870

1.1.0 Update to allow resizeable domains
https://doi.org/10.5281/zenodo.3766979

D.3 nanoHUB cloud-hosted model

The cloud-hosted deployment of the agent-based model (see Section D.2) can be accessed and run for free at

https://nanohub.org/tools/pc4livermedium.

The source code is available as open source under the 3-clause BSD license at

https://github.com/yafeiwang89/liver_medium

Zenodo archives

1.3 Source code for nanoHUB app version 1.3
http://doi.org/10.5281/zenodo.3775924

References

1. Siegel RL, Miller KD, Fedewa SA, Ahnen DJ, Meester RG, Barzi A, et al. Colorectal cancer statistics. CA: A cancer journal for clinicians. 2017;67(3):177–193. Available from: https://doi.org/10.3322/caac.21395.
2. Butcher DT, Alliston T, Weaver VM. A tense situation: forcing tumour progression. Nat Rev Cancer. 2009;9(2):108–22. Available from: https://doi.org/10.1038/nrc2544.
3. Cox TR, Erler JT. Remodeling and homeostasis of the extracellular matrix: implications for fibrotic diseases and cancer. Disease models & mechanisms. 2011;4(2):165–178. Available from: https://doi.org/10.1242/dmm.004077.
4. Hunt NJ, Kang SWS, Lockwood GP, Le Couteur DG, Cogger VC. Hallmarks of Aging in the Liver. Computational and Structural Biotechnology Journal. 2019;17:1151 – 1161. Available from: https://doi.org/10.1016/j.csbj.2019.07.021.
5. Phillip JM, Aifuwa I, Walston J, Wirtz D. The Mechanobiology of Aging. Annual Review of Biomedical Engineering. 2015;17(1):113–141. PMID: 26643020. Available from: https://doi.org/10.1146/annurev-bioeng-071114-040829.
6. Kim IH, Kisseleva T, Brenner DA. Aging and liver disease. Current Opinion in Gastroenterology. 2015;31(3):184–91. Available from: https://doi.org/10.1097/MOG.0000000000000176.
7. Ramia JM, López-Andujar R, Torras J, Falgueras L, Gonzalez JA, Sanchez B, et al. Multicentre study of liver metastases from colorectal cancer in pathological livers. HPB. 2011;13(5):320–3. Available from: https://doi.org/10.1111/j.1477-2574.2010.00287.x.
8. Chiou WY, Chang CM, Tseng KC, Hung SK, Lin HY, Chen YC, et al. Effect of liver cirrhosis on metastasis in colorectal cancer patients: a nationwide population-based cohort study. Japanese Journal of Clinical Oncology. 2014 11;45(2):160–168. Available from: https://doi.org/10.1093/jjco/hyu178.
9. Dong Y, Zheng Q, Wang Z, Lin X, You Y, Wu S, et al. Higher matrix stiffness as an independent initiator triggers epithelial-mesenchymal transition and facilitates HCC metastasis. Journal of Hematology & Oncology. 2019;12(1):112. Available from: https://doi.org/10.1186/s13045-019-0795-5.
10. Banyard J, Bielenberg DR. The role of EMT and MET in cancer dissemination. Connective Tissue Research. 2015;56(5):403–413. PMID: 26291767. Available from: https://doi.org/10.3109/03008207.2015.1060970.
11. Pickup MW, Mouw JK, Weaver VM. The extracellular matrix modulates the hallmarks of cancer. EMBO reports. 2014;15(12):1243–1253. Available from: https://doi.org/10.15252/embr.201439246.
12. Barney L, Jansen L, Polio S, Galarza S, Lynch M, Peyton S. The predictive link between matrix and metastasis. Current Opinion in Chemical Engineering. 2016;11:85–93. Biological Engineering / Material Engineering. Available from: https://doi.org/10.1016/j.coche.2016.01.001.

13. Schmucker DL. Age-related changes in liver structure and function: Implications for disease ? Experimental Gerontology. 2005;40(8):650 – 659. Available from: https://doi.org/10.1016/j.exger.2005.06.009.
14. Trefts E, Gannon M, Wasserman DH. The liver. Current Biology. 2017;27(21):R1147 – R1151. Available from: https://doi.org/10.1016/j.cub.2017.09.019.
15. Brunt EM, Gouw AS, Hubscher SG, Tiniakos DG, Bedossa P, Burt AD, et al. Pathology of the liver sinusoids. Histopathology. 2014;64(7):907–920. Available from: https://doi.org/10.1111/his.12364.
16. de Oliveira Lemos F, Florentino RM, Melo Lima Filho AC, dos Santos ML, Leite MF. Inositol 1,4,5-trisphosphate receptor in the liver: Expression and function. World J Gastroenterol. 2019;25(44):6483–94. Available from: https://doi.org/10.3748/wjg.v25.i44.6483.
17. Uhlén M, Fagerberg L, Hallström BM, Lindskog C, Oksvold P, Mardinoglu A, et al. Tissue-based map of the human proteome. Science. 2015;347(6220):1260419. Available from: https://doi.org/10.1126/science.1260419.
18. Brodt P. Role of the microenvironment in liver metastasis: from pre-to prometastatic niches. Clinical Cancer Research. 2016;22(24):5971–5982. Available from: https://doi.org/10.1158/1078-0432.CCR-16-0460.
19. Hoehme S, Brulport M, Bauer A, Bedawy E, Schormann W, Hermes M, et al. Prediction and validation of cell alignment along microvessels as order principle to restore tissue architecture in liver regeneration. Proceedings of the National Academy of Sciences. 2010;107(23):10371–10376. Available from: https://doi.org/10.1073/pnas.0909374107.
20. Van Liedekerke P, Neitsch J, Johann T, Warmt E, Grosser S, Valverde IG, et al. Quantifying the mechanics and growth of cells and tissues in 3D using high resolution computational models. bioRxiv. 2018;p. 470559. Available from: https://doi.org/10.1101/470559.
21. Friedman A, Hao W. Mathematical modeling of liver fibrosis. Mathematical Biosciences & Engineering. 2017;14(1):143–164. Available from: https://doi.org/10.3934/mbe.2017010.
22. Dutta-Moscato J, Solovyev A, Mi Q, Nishikawa T, Soto-Gutierrez A, Fox IJ, et al. A multiscale agent-based in silico model of liver fibrosis progression. Frontiers in bioengineering and biotechnology. 2014;2:18. Available from: https://doi.org/10.3389/fbioe.2014.00018.
23. Schwen LO, Schenk A, Kreutz C, Timmer J, Rodriguez MMB, Kuepfer L, et al. Representative sinusoids for hepatic four-scale pharmacokinetics simulations. PloS one. 2015;10(7):e0133653. Available from: https://doi.org/10.1371/journal.pone.0133653.
24. Sluka JP, Fu X, Swat M, Belmonte JM, Cosmanescu A, Clendenon SG, et al. A liver-centric multiscale modeling framework for xenobiotics. PloS one. 2016;11(9):e0162428. Available from: https://doi.org/10.1371/journal.pone.0162428.
25. Rani H, Sheu TW, Chang T, Liang P. Numerical investigation of non-Newtonian microcirculatory blood flow in hepatic lobule. Journal of biomechanics. 2006;39(3):551–563. Available from: https://doi.org/10.1016/j.jbiomech.2004.11.029.
26. Lettmann KA, Hardtke-Wolenski M. The importance of liver microcirculation in promoting autoimmune hepatitis via maintaining an inflammatory cytokine milieu–A mathematical model study. Journal of theoretical biology. 2014;348:33–46. Available from: https://doi.org/10.1016/j.jtbi.2014.01.016.
27. Siggers JH, Leungchavaphongse K, Ho CH, Repetto R. Mathematical model of blood and interstitial flow and lymph production in the liver. Biomechanics and modeling in mechanobiology. 2014;13(2):363–378. Available from: https://doi.org/10.1007/s10237-013-0516-x.
28. Ricken T, Werner D, Holzhütter H, König M, Dahmen U, Dirsch O. Modeling function–perfusion behavior in liver lobules including tissue, blood, glucose, lactate and glycogen by use of a coupled two-scale PDE–ODE approach. Biomechanics and modeling in mechanobiology. 2015;14(3):515–536. Available from: https://doi.org/10.1007/s10237-014-0619-z.

29. White D, Coombe D, Rezania V, Tuszynski J. Building a 3D virtual liver: Methods for simulating blood flow and hepatic clearance on 3D structures. PloS one. 2016;11(9):e0162215. Available from: https://doi.org/10.1371/journal.pone.0162215.
30. Nishii K, Reese G, Moran EC, Sparks JL. Multiscale computational model of fluid flow and matrix deformation in decellularized liver. Journal of the mechanical behavior of biomedical materials. 2016;57:201–214. Available from: https://doi.org/10.1016/j.jmbbm.2015.11.033.
31. Meyer K, Ostrenko O, Bourantas G, Morales-Navarrete H, Porat-Shliom N, Segovia-Miranda F, et al. A predictive 3D multi-scale model of biliary fluid dynamics in the liver lobule. Cell systems. 2017;4(3):277–290. Available from: https://doi.org/10.1016/j.cels.2017.02.008.
32. Ambrosi D, Preziosi L. Cell adhesion mechanisms and stress relaxation in the mechanics of tumours. Biomechanics and modeling in mechanobiology. 2009;8(5):397. Available from: https://doi.org/10.1007/s10237-008-0145-y.
33. Preziosi L, Ambrosi D, Verdier C. An elasto-visco-plastic model of cell aggregates. Journal of theoretical biology. 2010;262(1):35–47. Available from: https://doi.org/10.1016/j.jtbi.2009.08.023.
34. D'Antonio G, Macklin P, Preziosi L. An agent-based model for elasto-plastic mechanical interactions between cells, basement membrane and extracellular matrix. Math Biosci Eng. 2013;10(1):75–101. Available from: http://dx.doi.org/10.3934/mbe.2013.10.75.
35. Van Liedekerke P, Neitsch J, Johann T, Alessandri K, Nassoy P, Drasdo D. Quantitative cell-based model predicts mechanical stress response of growing tumor spheroids over various growth conditions and cell lines. PLoS computational biology. 2019;15(3):e1006273. Available from: https://doi.org/10.1371/journal.pcbi.1006273.
36. Cheng G, Tse J, Jain RK, Munn LL. Micro-environmental mechanical stress controls tumor spheroid size and morphology by suppressing proliferation and inducing apoptosis in cancer cells. PLoS one. 2009;4(2):e4632. Available from: https://doi.org/10.1371/journal.pone.0004632.
37. Voutouri C, Mpekris F, Papageorgis P, Odysseos AD, Stylianopoulos T. Role of constitutive behavior and tumor-host mechanical interactions in the state of stress and growth of solid tumors. PloS one. 2014;9(8):e104717. Available from: https://doi.org/10.1371/journal.pone.0104717.
38. Campbell A, Sivakumaran T, Davidson M, Lock M, Wong E. Mathematical modeling of liver metastases tumour growth and control with radiotherapy. Physics in Medicine & Biology. 2008;53(24):7225. Available from: https://doi.org/10.1088/0031-9155/53/24/015.
39. Haeno H, Gonen M, Davis MB, Herman JM, Iacobuzio-Donahue CA, Michor F. Computational modeling of pancreatic cancer reveals kinetics of metastasis suggesting optimum treatment strategies. Cell. 2012;148(1-2):362–375. Available from: https://doi.org/10.1016/j.cell.2011.11.060.
40. Bethge A, Schumacher U, Wedemann G. Simulation of metastatic progression using a computer model including chemotherapy and radiation therapy. Journal of biomedical informatics. 2015;57:74–87. Available from: https://doi.org/10.1016/j.jbi.2015.07.011.
41. Hudson SV, Dolin CE, Poole LG, Massey VL, Wilkey D, Beier JI, et al. Modeling the kinetics of integrin receptor binding to hepatic extracellular matrix proteins. Scientific reports. 2017;7(1):12444. Available from: https://doi.org/10.1038/s41598-017-12691-y.
42. Mahlbacher G, Curtis LT, Lowengrub J, Frieboes HB. Mathematical modeling of tumor-associated macrophage interactions with the cancer microenvironment. Journal for immunotherapy of cancer. 2018;6(1):10. Available from: https://doi.org/10.1186/s40425-017-0313-7.
43. Hudson SV, Miller HA, Mahlbacher GE, Saforo D, Beverly LJ, Arteel GE, et al. Computational/experimental evaluation of liver metastasis post hepatic injury: interactions with macrophages and transitional ECM. Scientific Reports. 2019;9(1):1–13. Available

from: https://doi.org/10.1038/s41598-019-51249-y.
44. Leonard F, Curtis LT, Yesantharao P, Tanei T, Alexander JF, Wu M, et al. Enhanced performance of macrophage-encapsulated nanoparticle albumin-bound-paclitaxel in hypo-perfused cancer lesions. Nanoscale. 2016;8(25):12544–12552. Available from: https://doi.org/10.1039/C5NR07796F.
45. Leonard F, Curtis LT, Ware MJ, Nosrat T, Liu X, Yokoi K, et al. Macrophage polarization contributes to the anti-Tumoral efficacy of Mesoporous Nanovectors loaded with albumin-bound Paclitaxel. Frontiers in immunology. 2017;8:693. Available from: https://doi.org/10.3389/fimmu.2017.00693.
46. Leonard F, Curtis LT, Hamed AR, Zhang C, Chau E, Sieving D, et al. Nonlinear response to cancer nanotherapy due to macrophage interactions revealed by mathematical modeling and evaluated in a murine model via CRISPR-modulated macrophage polarization. Cancer Immunology Immunotherapy. 2020;69:731–744. Available from: https://10.1007/s00262-020-02504-z.
47. Curtis LT, Rychahou P, Bae Y, Frieboes HB. A Computational/Experimental Assessment of Antitumor Activity of Polymer Nanoassemblies for pH-Controlled Drug Delivery to Primary and Metastatic Tumors. Pharmaceutical Research. 2016;33:2552–2564. Available from: https://10.1007/s11095-016-1981-6.
48. Reichel D, Curtis LT, Ehlman E, Evers BM, Rychahou P, Frieboes HB, et al. Development of Halofluorochromic Polymer Nanoassemblies for the Potential Detection of Liver Metastatic Colorectal Cancer Tumors Using Experimental and Computational Approaches. Pharmaceutical Research. 2017;34:2385–2402. Available from: https://10.1007/s11095-017-2245-9.
49. Haeno H, Michor F. The evolution of tumor metastases during clonal expansion. Journal of theoretical biology. 2010;263(1):30–44. Available from: https://doi.org/10.1016/j.jtbi.2009.11.005.
50. Newton PK, Mason J, Bethel K, Bazhenova LA, Nieva J, Kuhn P. A stochastic Markov chain model to describe lung cancer growth and metastasis. PloS one. 2012;7(4):e34637. Available from: https://doi.org/10.1371/journal.pone.0034637.
51. Scott JG, Basanta D, Anderson AR, Gerlee P. A mathematical model of tumour self-seeding reveals secondary metastatic deposits as drivers of primary tumour growth. Journal of The Royal Society Interface. 2013;10(82):20130011. Available from: https://doi.org/10.1098/rsif.2013.0011.
52. Newton PK, Mason J, Bethel K, Bazhenova L, Nieva J, Norton L, et al. Spreaders and sponges define metastasis in lung cancer: a Markov chain Monte Carlo mathematical model. Cancer research. 2013;73(9):2760–2769. Available from: https://doi.org/10.1158/0008-5472.CAN-12-4488.
53. Scott JG, Fletcher AG, Maini PK, Anderson AR, Gerlee P. A filter-flow perspective of haematogenous metastasis offers a non-genetic paradigm for personalised cancer therapy. European journal of cancer. 2014;50(17):3068–3075. Available from: https://doi.org/10.1016/j.ejca.2014.08.019.
54. Newton PK, Mason J, Venkatappa N, Jochelson MS, Hurt B, Nieva J, et al. Spatiotemporal progression of metastatic breast cancer: a Markov chain model highlighting the role of early metastatic sites. NPJ breast cancer. 2015;1:15018. Available from: https://doi.org/10.1038/npjbcancer.2015.18.
55. Deng J, Wei W, Chen Z, Lin B, Zhao W, Luo Y, et al. Engineered Liver-On-A-Chip Platform to Mimic Liver Functions and Its Biomedical Applications: A Review. Micromachines. 2019;10(10). Available from: https://www.mdpi.com/2072-666X/10/10/676.
56. Wheeler SE, Clark AM, Taylor DP, Young CL, Pillai VC, Stolz DB, et al. Spontaneous dormancy of metastatic breast cancer cells in an all human liver microphysiologic system. Br J Cancer. 2014;111(12):2342–50. Available from: https://doi.org/10.1038/bjc.2014.533.
57. Simon BR. Multiphase poroelastic finite element models for soft tissue structures. Applied Mechanics Reviews. 1992;45(6):191–218. Available from: https://doi.org/10.1115/1.3121397.
58. Raghunathan S, Evans D, Sparks JL. Poroviscoelastic modeling of liver biomechanical response in unconfined compression. Annals of biomedical

engineering. 2010;38(5):1789–1800. Available from: https://doi.org/10.1007/s10439-010-9957-x.
59. Moran EC, Raghunathan S, Evans DW, Vavalle NA, Sparks JL, LeRoith T, et al. Poro-hyperviscoelastic model simultaneously predicts parenchymal fluid pressure and reaction force in perfused liver. Journal of biomechanical engineering. 2012;134(9):091002. Available from: https://doi.org/10.1115/1.4007175.
60. Evans DW, Moran EC, Baptista PM, Soker S, Sparks JL. Scale-dependent mechanical properties of native and decellularized liver tissue. Biomechanics and modeling in mechanobiology. 2013;12(3):569–580. Available from: https://doi.org/10.1007/s10237-012-0426-3.
61. Athanasiou KA, Natoli RM. Introduction to continuum biomechanics. Synthesis lectures on biomedical engineering. 2008;3(1):1–206. Available from: https://doi.org/10.2200/S00121ED1V01Y200805BME019.
62. Mow VC, Kuei S, Lai WM, Armstrong CG. Biphasic creep and stress relaxation of articular cartilage in compression: theory and experiments. Journal of biomechanical engineering. 1980;102(1):73–84. Available from: https://doi.org/10.1115/1.3138202.
63. Mak A. The apparent viscoelastic behavior of articular cartilage—the contributions from the intrinsic matrix viscoelasticity and interstitial fluid flows. Journal of biomechanical engineering. 1986;108(2):123–130. Available from: https://doi.org/10.1115/1.3138591.
64. Suh JK, Bai S. Finite element formulation of biphasic poroviscoelastic model for articular cartilage. Journal of biomechanical engineering. 1998;120(2):195–201. Available from: https://doi.org/10.1115/1.2798302.
65. Carbrey JM, Gorelick-Feldman DA, Kozono D, Praetorius J, Nielsen S, Agre P. Aquaglyceroporin AQP9: solute permeation and metabolic control of expression in liver. Proceedings of the National Academy of Sciences. 2003;100(5):2945–2950. Available from: https://doi.org/10.1073/pnas.0437994100.
66. Ismail MF, Ali DA, Fernando A, Abdraboh ME, Gaur RL, Ibrahim WM, et al. Chemoprevention of rat liver toxicity and carcinogenesis by Spirulina. International journal of biological sciences. 2009;5(4):377. Available from: https://doi.org/10.7150/ijbs.5.377.
67. Debbaut C, Vierendeels J, Casteleyn C, Cornillie P, Van Loo D, Simoens P, et al. Perfusion characteristics of the human hepatic microcirculation based on three-dimensional reconstructions and computational fluid dynamic analysis. Journal of biomechanical engineering. 2012;134(1):011003. Available from: https://doi.org/10.1115/1.4005545.
68. Ren H, Shi X, Tao L, Xiao J, Han B, Zhang Y, et al. Evaluation of two decellularization methods in the development of a whole-organ decellularized rat liver scaffold. Liver International. 2013;33(3):448–458. Available from: https://doi.org/10.1111/liv.12088.
69. Ghaffarizadeh A, Friedman SH, Macklin P. BioFVM: an efficient, parallelized diffusive transport solver for 3-D biological simulations. Bioinformatics. 2016;32(8):1256–8. Available from: http://dx.doi.org/10.1093/bioinformatics/btv730.
70. Ghaffarizadeh A, Heiland R, Friedman SH, Mumenthaler SM, Macklin P. PhysiCell: an open source physics-based cell simulator for 3-D multicellular systems. PLoS Comput Biol. 2018;14(2):e1005991. Available from: http://dx.doi.org/10.1371/journal.pcbi.1005991.
71. Hoehme S, Drasdo D. A cell-based simulation software for multi-cellular systems. Bioinformatics. 2010;26(20):2641–2642. Available from: https://doi.org/10.1093/bioinformatics/btq437.
72. Heiland R, Mishler D, Zhang T, Bower E, Macklin P. xml2jupyter: Mapping parameters between XML and Jupyter widgets. Journal of Open Source Software. 2019;4(39):1408. Available from: http://dx.doi.org/10.21105/joss.01408.
73. Madhavan K, Zentner L, Farnsworth V, Shivarajapura S, Zentner M, Denny N, et al. nanoHUB. org: Cloud-based services for nanoscale modeling, simulation, and education. Nanotechnology Reviews. 2013;2(1):107–117. Available from: https://doi.org/10.1515/ntrev-2012-0043.

74. Wang Y, Heiland R, Macklin P. PhysiCell: liver tissue mechanobiology. nanoHUB; 2019. Available from: https://nanohub.org/resources/pc4livermedium.
75. Tsukada K, Suematsu M. Visualization and Analysis of Blood Flow and Oxygen Consumption in Hepatic Microcirculation: Application to an Acute Hepatitis Model. J Vis Exp. 2012;66:e3996. Available from: http://dx.doi.org/10.3791/3996.
76. Macklin P, Lowengrub JS. Nonlinear simulation of the effect of microenvironment on tumor growth. J Theor Biol. 2007;245(4):677–704. Available from: http://dx.doi.org/10.1016/j.jtbi.2006.12.004.
77. Macklin P, Lowengrub JS. A New Ghost Cell/Level Set Method for Moving Boundary Problems: Application to Tumor Growth. J Sci Comput. 2008;35(2-3):266–299. (invited author: J.S. Lowengrub). Available from: http://dx.doi.org/10.1007/s10915-008-9190-z.
78. Lowengrub J, Frieboes HB, Jin F, Chuang YL, Li X, Macklin P, et al. Nonlinear modelling of cancer: Bridging the gap between cells and tumors. Nonlinearity. 2010;23(1):R1–R91. (invited author: J. Lowengrub). Available from: http://dx.doi.org/10.1088/0951-7715/23/1/R01.
79. Van Liedekerke P, Neitsch J, Johann T, Alessandri K, Nassoy P, Drasdo D. Quantitative cell-based model predicts mechanical stress response of growing tumor spheroids over various growth conditions and cell lines. PLOS Computational Biology. 2019 03;15(3):1–40. Available from: https://doi.org/10.1371/journal.pcbi.1006273.
80. Stylianopoulos T, Martin JD, Snuderl M, Mpekris F, Jain SR, Jain RK. Coevolution of solid stress and interstitial fluid pressure in tumors during progression: implications for vascular collapse. Cancer research. 2013;73(13):3833–3841. Available from: https://doi.org/10.1158/0008-5472.CAN-12-4521.
81. Streichan SJ, Hoerner CR, Schneidt T, Holzer D, Hufnagel L. Spatial constraints control cell proliferation in tissues. Proceedings of the National Academy of Sciences. 2014;111(15):5586–5591. Available from: https://www.pnas.org/content/111/15/5586.
82. Brás-Pereira C, Moreno E. Mechanical cell competition. Current Opinion in Cell Biology. 2018;51:15 – 21. Cell Signalling. Available from: http://www.sciencedirect.com/science/article/pii/S0955067417300765.
83. Byrne H, Drasdo D. Individual-based and continuum models of growing cell populations: a comparison. J Theor Biol. 2008;58(4):657–87. Available from: https://doi.org/10.1007/s00285-008-0212-0.
84. Marmottant P, Mgharbel A, Käfer J, Audren B, Rieu JP, Vial JC, et al. The role of fluctuations and stress on the effective viscosity of cell aggregates. Proceedings of the National Academy of Sciences. 2009;106(41):17271–17275. Available from: https://doi.org/10.1073/pnas.0902085106.
85. Friedman SH, Anderson ARA, Bortz DM, Fletcher AG, Frieboes HB, Ghaffarizadeh A, et al. MultiCellDS: a standard and a community for sharing multicellular data. bioRxiv. 2016;090696. (preprint, in revision). Available from: http://dx.doi.org/10.1101/090696.
86. Helmlinger G, Netti PA, Lichtenbeld HC, Melder RJ, Jain RK. Solid stress inhibits the growth of multicellular tumor spheroids. Nature biotechnology. 1997;15(8):778–783. Available from: https://doi.org/10.1038/nbt0897-778.
87. Boire A, Coffelt SB, Quezada SA, Vander Heiden MG, Weeraratna AT. Tumour Dormancy and Reawakening: Opportunities and Challenges. Trends in Cancer. 2019;5:762–5. Available from: https://doi.org/10.1016/j.trecan.2019.10.010.
88. Clark AM, Wheeler SE, Young CL, Stockdale L, Shepard Neiman J, Zhao W, et al. A liver microphysiological system of tumor cell dormancy and inflammatory responsiveness is affected by scaffold properties. Lab Chip. 2017;17:156–168. Available from: http://dx.doi.org/10.1039/C6LC01171C.
89. Bertolotti M, Lonardo A, Mussi C, Baldelli E, Pellegrini E, Ballestri S, et al. Nonalcoholic fatty liver disease and aging: Epidemiology to management. World J Gastroenterol. 2014;20(39):14185–204. Available from: https://www.wjgnet.com/1007-9327/full/v20/i39/14185.htm.
90. Fane M, Weeraratna AT. How the ageing microenvironment influences tumour progression. Nat Rev Cancer. 2020;20(2):89–106. Available from: https://doi.org/10.

1038/s41568-019-0222-9.

91. Patsenker E, Stickel F. Role of integrins in fibrosing liver diseases. Am J of Physiology-Gastrointestinal and Liver Physiology. 2011;301(3):G425–G434. PMID: 21659620. Available from: https://doi.org/10.1152/ajpgi.00050.2011.
92. Levental KR, Yu H, Kass L, Lakins JN, Egeblad M, Erler JT, et al. Matrix Crosslinking Forces Tumor Progression by Enhancing Integrin Signaling. Cell. 2009;139(5):891–906. Available from: https://doi.org/10.1016/j.cell.2009.10.027.
93. Wang H, Abhilash AS, Chen C, Wells R, Shenoy V. Long-Range Force Transmission in Fibrous Matrices Enabled by Tension-Driven Alignment of Fibers. Biophys J. 2014;107(11):2592–603. Available from: https://doi.org/10.1016/j.bpj.2014.09.044.
94. Mavrogonatou E, Pratsinis H, Papadopoulou A, Karamanos NK, Kletsas D. Extracellular matrix alterations in senescent cells and their significance in tissue homeostasis. Matrix Biology. 2019;75-76:27 – 42. Matrix Modeling and Remodeling. Available from: http://www.sciencedirect.com/science/article/pii/S0945053X17302962.
95. Jiang D, Lim SY. Influence of Immune Myeloid Cells on the Extracellular Matrix During Cancer Metastasis. Cancer Microenvironment. 2016 Apr;9(1):45–61. Available from: https://doi.org/10.1007/s12307-016-0181-6.
96. Kaur A, Ecker BL, Douglass SM, Kugel CH, Webster MR, Almeida FV, et al. Remodeling of the Collagen Matrix in Aging Skin Promotes Melanoma Metastasis and Affects Immune Cell Motility. Cancer Discovery. 2019;9(1):64–81. Available from: https://cancerdiscovery.aacrjournals.org/content/9/1/64.
97. Ahmadzadeh H, Webster MR, Behera R, Jimenez Valencia AM, Wirtz D, Weeraratna AT, et al. Modeling the two-way feedback between contractility and matrix realignment reveals a nonlinear mode of cancer cell invasion. Proceedings of the National Academy of Sciences. 2017;114(9):E1617–E1626. Available from: https://www.pnas.org/content/114/9/E1617.
98. Metzcar J, Wang Y, Heiland R, Macklin P. A review of cell-based computational modeling in cancer biology. JCO Clinical Cancer Informatics. 2019;3:1–13. (invited review). Available from: http://dx.doi.org/10.1200/CCI.18.00069.
99. Chamseddine IM, Rejniak KA. Hybrid modeling frameworks of tumor development and treatment. WIREs Systems Biology and Medicine. 2020;12(1):e1461. Available from: https://onlinelibrary.wiley.com/doi/abs/10.1002/wsbm.1461.
100. Baratchart E, Benzekry S, Bikfalvi A, Colin T, Cooley LS, Pineau R, et al. Computational modelling of metastasis development in renal cell carcinoma. PLoS computational biology. 2015;11(11):e1004626. Available from: https://doi.org/10.1371/journal.pcbi.1004626.
101. Malek A. Experimental metastasis: modeling and analysis. Springer; 2013.